J. Fluid Mech. (2023), *vol*. 954, A39, doi:10.1017/jfm.2022.1028

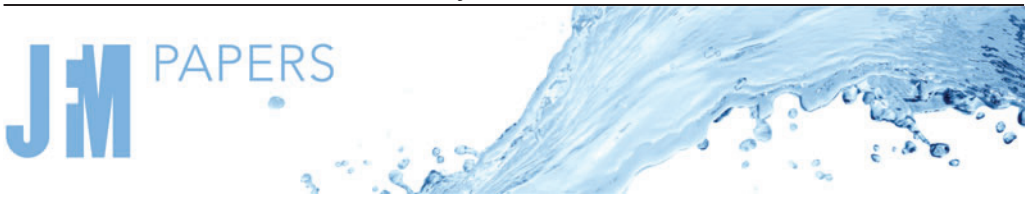

Droplet size distribution in a swirl airstream using in-line holography technique

Someshwar Sanjay Ade[1], **Pavan Kumar Kirar**[2], **Lakshmana Dora Chandrala**[3],† **and Kirti Chandra Sahu**[2],†

[1]Center for Interdisciplinary Program, Indian Institute of Technology Hyderabad, Kandi, Sangareddy 502 284, Telangana, India

[2]Department of Chemical Engineering, Indian Institute of Technology Hyderabad, Kandi, Sangareddy 502 284, Telangana, India

[3]Department of Mechanical and Aerospace Engineering, Indian Institute of Technology Hyderabad, Kandi, Sangareddy 502 284, Telangana, India

(Received 7 July 2022; revised 30 November 2022; accepted 3 December 2022)

We investigate the morphology and size distribution of satellite droplets resulting from the interaction of a freely falling water droplet with a swirling airstream of different strengths by employing shadowgraphy and deep-learning-based digital in-line holography techniques. We found that the droplet exhibits vibrational, retracting bag and normal breakup phenomena for the no swirl, low and high swirl strengths for the same aerodynamic field. In the high-swirl scenario, the disintegrations of the nodes, rim and bag-film contribute to the number mean diameter, resulting in smaller satellite droplets. In contrast, in the low-swirl case, the breakup of the rim and nodes only contributes to the size distribution, resulting in larger droplets. The temporal variation of the Sauter mean diameter reveals that for a given aerodynamic force, a high swirl strength produces more surface area and surface energy than a low swirl strength. The theoretical prediction of the number-mean probability density of tiny satellite droplets under swirl conditions agrees with experimental data. However, for the low swirl, the predictions differ from the experimental results, particularly due to the presence of large satellite droplets. Our results reveal that the volume-weighted droplet size distribution exhibits two (bi-modal) and three (multi-model) peaks for low and high swirl strengths, respectively. The analytical model that takes into account various mechanisms, such as the nodes, rim and bag breakups, accurately predicts the shape and characteristic sizes of each mode for the case of high swirl strength.

Key words: breakup/coalescence, drops

† Email addresses for correspondence: lchandrala@mae.iith.ac.in, ksahu@che.iith.ac.in

1. Introduction

Raindrops reach earth in a variety of shapes and sizes due to their complex interactions with the atmosphere and accompanying microphysical processes, such as fragmentation (Kostinski & Shaw 2009; Villermaux & Bossa 2009), coalescence (Schlottke & Weigand 2008; Chaitanya, Sahu & Biswas 2021) and phase change (Schlottke & Weigand 2008). These microphysical processes are further influenced by various factors, including meteorological conditions, cloud type from which raindrops originate, the topology of the earth and air movement in the atmosphere. The distribution of shape and size of raindrops is one of the important factors in rainfall modelling. This was first noticed by Bentley (1904) and von Lenard (1904). Subsequently, Marshall & Palmer (1948) established a relationship that correlates the average diameter of raindrops with rainfall rate, which has been used in rainfall modelling even today (Villermaux & Bossa 2009). Although several researchers have studied the droplet fragmentation phenomenon due to its importance in a variety of industrial applications, such as combustion, surface coating, pharmaceutical manufacturing and disease transmission modelling (Marmottant & Villermaux 2004; Villermaux 2007; Soni *et al.* 2020; Jackiw & Ashgriz 2021; Kirar *et al.* 2022; Xu, Wang & Che 2022), there have been very few studies on the size distribution of satellite droplets after fragmentation of a large droplet (Srivastava 1971; Villermaux & Bossa 2009; Gao *et al.* 2022; Jackiw & Ashgriz 2022). Moreover, to our knowledge, no one has previously investigated the droplet size distribution under swirl airstream, even though such a situation is frequently encountered during rainfall (Lewellen, Lewellen & Xia 2000; Haan *et al.* 2017) and in many industrial applications (Soni & Kolhe 2021; Candel *et al.* 2014). This is the subject of the present investigation.

In a continuous airstream, a droplet undergoes morphological changes due to the development of the Rayleigh–Taylor instability during its early inflation stage and later encounters fragmentation due to the Rayleigh–Plateau capillary instability (Taylor 1963) and nonlinear instability of liquid ligaments (Jackiw & Ashgriz 2021, 2022). The droplet exhibits different breakup modes, such as vibrational, bag, bag-stamen, multi-bag, shear and catastrophic breakup modes, depending on the speed and direction of the airstream (Pilch & Erdman 1987; Dai & Faeth 2001; Cao *et al.* 2007; Guildenbecher, López-Rivera & Sojka 2009; Suryaprakash & Tomar 2019; Soni *et al.* 2020). The Weber number, defined as $We \equiv \rho_a U^2 d_0/\sigma$, wherein ρ_a, σ, U and d_0 denote the density of the air, interfacial tension, average velocity of the airstream and equivalent spherical diameter of the droplet, is used to characterize the droplet breakup phenomenon. A droplet exhibits shape oscillations at a specific frequency for low Weber numbers and fragments into small droplets of comparable size. This is known as the vibrational breakup. As the Weber number is increased, the droplet evolves to form a single bag on the leeward side, encircled by a thick liquid rim. As a result of the bag and rim fragmentation, tiny and slightly bigger droplets are formed. This process is known as the bag breakup phenomenon. The bag-stamen and multi-bag morphologies are identical to the bag breakup mode, but with a stamen formation in the drop's centre, resulting in a large additional drop during the breakup (bag-stamen fragmentation) and several bags formation (multi-bag mode fragmentation). In shear mode, the drop's edge deflects downstream, fracturing the sheet into small droplets. When the Weber number is exceedingly high, the droplet explodes into a cluster of tiny fragments very quickly, resulting in catastrophic fragmentation. Taylor (1963) was the first to find the critical Weber number (We_{cr}) at which the transition from the vibrational to the bag breakup occurs. Subsequently, several researchers have investigated droplet fragmentation subjected to an airstream in cross-flow configuration (when the droplet interacts with the airstream in a direction orthogonal to gravity) and

in-line configurations, such as co-flow and oppose-flow, when the droplet interacts with the airstream flowing along and opposite to the direction of gravity, respectively. The critical Weber numbers in cross-flow (Krzeczkowski 1980; Pilch & Erdman 1987; Wierzba 1990; Hsiang & Faeth 1993; Guildenbecher *et al.* 2009; Kulkarni & Sojka 2014; Wang *et al.* 2014; Jain *et al.* 2015) and oppose-flow (Villermaux & Bossa 2009; Villermaux & Eloi 2011) configurations were found to be approximately 12 and 6, respectively. Soni *et al.* (2020) showed that in the case of an oblique airstream, a freely falling droplet exhibits curvilinear motion while undergoing topological changes and that the critical Weber number decreases when the direction of the airstream changes from the cross-flow to the oppose-flow condition. The value of We_{cr} was found to be approximately 12 in the cross-flow configuration, and its value approaches 6 when the inclination angle of the airstream with the horizontal is greater than 60°. The initial droplet size, fluid properties, ejection height from the nozzle and velocity profile/potential core region are also known to affect the critical Weber number (Hanson, Domich & Adams 1963; Wierzba 1990). All these investigations are for straight airflow in the no-swirl condition. The deformation and breakup of a water droplet falling in air have also been investigated (Szakall *et al.* 2009; Agrawal *et al.* 2017; Balla, Tripathi & Sahu 2019; Agrawal *et al.* 2020).

A few researchers (Merkle *et al.* 2003; Rajamanickam & Basu 2017; Kumar & Sahu 2019; Patil & Sahu 2021; Soni & Kolhe 2021) have examined the characteristics of swirl flow using high-speed imaging and particle image velocimetry (PIV) techniques. The droplet morphology and breakup phenomenon in a swirling airflow is more complex than in a straight airflow without a swirl. In the case of swirl airflow, the droplet encounters oppose-flow, cross-flow and co-flow situations simultaneously, depending on its ejection position, airstream velocity and swirl strength. Recently, Kirar *et al.* (2022) experimentally analysed the droplet fragmentation phenomenon under a swirling airstream using shadowgraphy and PIV techniques. They discovered a new breakup mode, termed as 'retracting bag breakup', due to the differential flow field created by the wake of the swirler's vanes and the central recirculation zone in swirl airflow. A theoretical analysis based on the Rayleigh–Taylor instability was also developed that uses a modified stretching factor to predict the droplet deformation process under a swirl airstream. Apte *et al.* (2009) performed large-eddy simulations of spray atomization from a swirl injector. They used a Pratt and Whitney injector (a high-bypass turbofan engine family) to create a spray alteration/rotation. They found that the number probability density of the atomized droplets follows the Fokker–Planck equation. This partial differential equation provides the temporal evolution of the probability distribution of the velocity of a particle subjected to drag and random forces similar to that in Brownian motion. Apart from the studies mentioned above, Shanmugadas *et al.* (2018) experimentally investigated wall filming and atomization from a swirl cup injector. The injector uses a simplex nozzle and a primary swirler to create a liquid rim and a secondary swirler to create the ligaments and droplets from the rim by shearing action. Their study reveals that the atomization/fragmentation process is a strong function of the central recirculation zone of the primary swirl. Further, Shao *et al.* (2018) performed direct numerical simulations on the swirling sheet breakup process leading to the formation of sheets, ligaments and droplets. They found that the size distribution of droplets in a swirling sheet breakup process approximately follows the log-normal distribution. As this discussion indicates, despite significant research on the various droplet breakup processes and flow characteristics in straight and swirling airstreams, the size distribution of satellite droplets following the fragmentation of a single droplet has not been investigated yet.

The size distribution of satellite droplets due to fragmentation is commonly analysed using laser diffraction (LD), phase Doppler particle analyser (PDPA) and in-line holography techniques (Katz & Sheng 2010; Gao *et al.* 2013*b*; Kumar *et al.* 2019). In the LD technique, a radial sensor measures the light scattered by the satellite droplets in the forward direction. This is not an imaging-based approach and must be used in conjunction with a model-based inversion to estimate the size distribution function of the detected droplets. The PDPA is a single-point measurement technique where the phase difference of scattered light captured at multiple angles is used to obtain the size of the droplets. The LD and PDPA techniques are suitable for applications, such as spray atomization, where droplets are produced continuously. However, both methods suffer from a number of limitations, such as small sampling volume in the PDPA method and lack of spatial resolution in the LD technique. Moreover, while the PDPA is restricted to spherical particles, the LD technique is not sensitive to single-droplet analysis.

In contrast, the digital in-line holography technique, which employs a deep-learning-based image processing method, has recently emerged as a powerful tool for capturing three-dimensional information about an object with a high spatial resolution (Shao *et al.* 2020). This technique can also offer the spatial distribution of satellite droplets. Thus, it is a superior choice to be used in the current study to analyse the size distribution of satellite droplets resulting from the fragmentation of a water droplet subjected to a swirl airstream. A few researchers have employed in-line holography to determine the droplet's size distribution in a straight airstream in no-swirl conditions. For instance, for an ethanol droplet in a cross-flowing airstream, Gao *et al.* (2013*b*) and Guildenbecher *et al.* (2017) used the in-line holography technique to obtain the three-dimensional position and velocities of fragments in the bag breakup and shear-thinning regimes. Li *et al.* (2022) used this technique to analyse the size distribution of satellite droplets under an induced shock wave. The investigation by Jackiw & Ashgriz (2022) is one of the most relevant studies in the context of the present work. Jackiw & Ashgriz (2022) developed an analytical model for the combined multi-modal distribution resulting from the aerodynamic breakup of a droplet under no-swirl conditions. They demonstrated that their theoretical predictions agree well with the experimental results of Guildenbecher *et al.* (2017). Although Jackiw & Ashgriz (2022) performed fragmentation experiments for a water droplet under straight airflow without swirling using a shadowgraphy technique, they only analysed the size distributions of satellite ethanol droplets reported by Guildenbecher *et al.* (2017) using a digital in-line holography technique.

In the present work, we investigate the size distribution of satellite droplets resulting from the fragmentation of a freely falling water droplet under a swirl airstream of different strengths by employing both shadowgraphy and digital in-line holography techniques. We found that while the satellite droplets show mono-modal size distribution for the no-swirl airstream, the fragmentation exhibits bi-modal and multi-modal distributions in a swirl flow for the low and high swirl strengths, respectively. A theoretical analysis accounting for various mechanisms, such as the nodes, rim and bag breakup mode, is also carried out to determine the size distribution of droplets for different swirl strengths. To the best of our knowledge, the present study is the first attempt to estimate the size distribution of satellite droplets under swirl airstreams, which are commonly observed in many natural and industrial applications.

The rest of the paper is organized as follows. In § 2, the experimental set-up and procedure for both the shadowgraph and digital in-line holography are elaborated. To demonstrate the digital in-line holography technique used in our work, we have considered a typical bag fragmentation of a water droplet under a straight airstream without swirl and compared our result with the size distribution of an ethanol droplet considered by

Guildenbecher *et al.* (2017). The influence of different swirl airstreams on the droplet fragmentation and the resulting size distribution are discussed in § 3. A theoretical model is employed to predict the size distributions of satellite droplets obtained from our in-line holography technique. The concluding remarks are given in § 4.

2. Experimental set-up

In the present study, while a shadowgraphy technique is employed to investigate the droplet deformation and breakup phenomena of a freely falling droplet under an imposed swirl airstream, a digital in-line holography technique is used to analyse the size distribution of satellite droplets after fragmentation of the primary drop. The experimental set-up consists of (i) an air nozzle (18 mm diameter) with a swirler, (ii) a droplet dispensing needle connected to a three-dimensional (3-D) traverse system, (iii) a continuous wave laser, (iv) a spatial filter arrangement, (v) collimating optics which include concave and convex lenses, (vi) two high-speed cameras and (vii) a diffused backlit illumination. A schematic diagram of the complete experimental set-up is shown in figure 1. The inset at the bottom of figure 1 shows the back and side views of the swirler. To change the strength of the swirl airstream, two different types of eight-vane swirlers are used, one with a vane angle, $\theta = 30^\circ$, and the other with $\theta = 45^\circ$. The rest of the dimensions of the swirlers are the same: outer diameter ($D_o = 22$ mm), inner diameter ($D_i = 20$ mm), dome diameter ($D_m = 12$ mm) and blade thickness (= 1 mm). The swirl strength is characterized by the geometric swirl number (Sw), which is defined as (Beér 1974)

$$Sw = \frac{2}{3}\left(\frac{1-(D_i/D_o)^3}{1-(D_i/D_o)^2}\right)\tan\theta, \tag{2.1}$$

such that when $\theta = 30^\circ$ and 45°, we achieve $Sw = 0.47$ (low swirl strength) and $Sw = 0.82$ (high swirl strength), respectively. We have also calculated the flow-based swirl number (Sw_f) using the stereo-PIV measurements (Kirar *et al.* 2022). The flow swirl number (Sw_f) is given by

$$Sw_f = \frac{\displaystyle\int_0^R u_y u_\theta r^2\,\mathrm{d}r}{R\displaystyle\int_0^R {u_y}^2 r\,\mathrm{d}r}, \tag{2.2}$$

where u_y and u_θ are the axial and tangential components of the velocity and R denotes the radius of the swirler (Candel *et al.* 2014). We found that the values of Sw_f are approximately 0.42 and 0.58 for the corresponding geometric swirl numbers $Sw = 0.47$ and 0.82, respectively.

The swirlers are fabricated with a tough resin using 3-D printing technology and have provision for attaching at the exit of a metallic circular nozzle. To remove inlet airstream disturbances and straighten the flow, a honeycomb pallet is placed upstream of the nozzle. The air nozzle is connected to an ALICAT digital mass flow controller (model, MCR-500SLPM-D/CM; make, Alicat Scientific, Inc., USA), which can regulate flow rates between 0 and 500 standard litres per minute. The accuracy of the flow metre is approximately 0.8 % of the reading +0.2 % of the full scale. The mass flow controller is coupled to an air compressor for air supply. An air dryer and moisture remover are installed in the compressed airline to maintain dry air during the experiments.

A Cartesian coordinate system (x, y, z) with its origin at the centre of the swirler tip, as shown in figure 1, is used to analyse the dynamics. A syringe pump (model, HO-SPLF-2D;

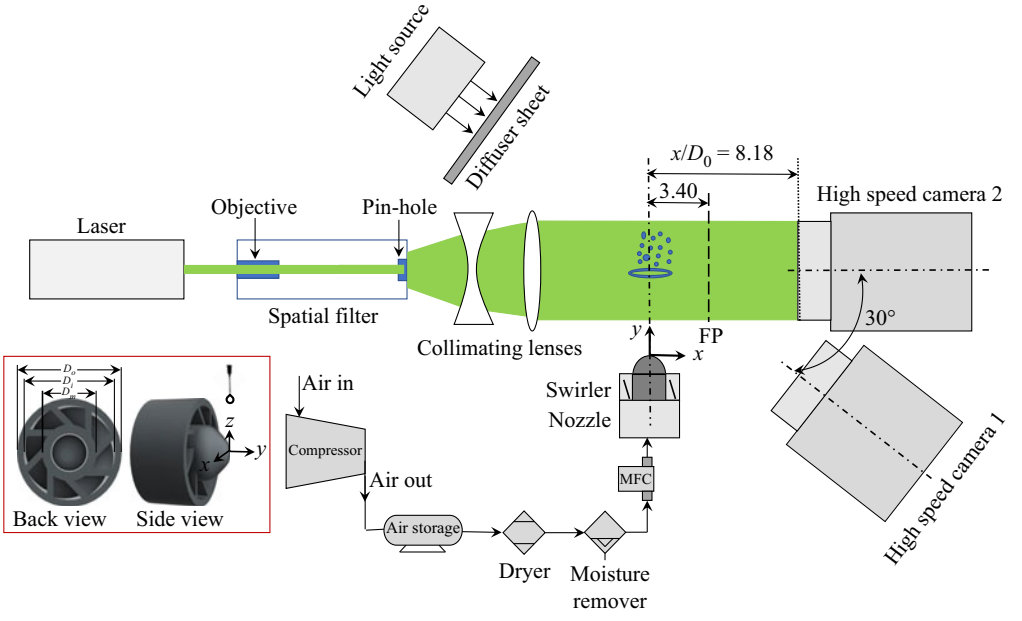

Figure 1. Schematic of the experimental set-up (top view) equipped with a shadowgraphy and digital in-line holography systems to investigate the size distribution of satellite droplets due to the fragmentation of a freely falling water droplet under an imposed swirl airstream. The inset depicts the back and side views of a swirler. Here, FP and MFC represent the focal plane associated with the high-speed camera 2 and mass flow controller, respectively. A picture of our experimental set-up is presented as figure S1 in the supplementary material available at https://doi.org/10.1017/jfm.2022.1028.

make, Holmarc Opto-Mechatronics Pvt. Ltd., India) connected to a dispensing needle is used to create consistent-sized droplets of water (spherical diameter, $d_0 = 3.09 \pm 0.07$ mm). We use a 20 Gauge needle to dispense the droplets. The outer and inner diameters of the needle are 0.908 mm and 0.603 mm, respectively, and the length of the needle is 25.4 mm. The dispensing needle is fixed to a three-dimensional traverse mechanism that allows it to change the location of its tip (x_d, y_d, z_d) and thus control the droplet's location in the swirl airstream. A flow rate of $20\,\mu l\,s^{-1}$ is maintained in the syringe pump to create a water droplet at the tip of a blunt needle. This flow rate is low enough that only gravity can detach the droplets from the needle. We ensure that no other droplets emerge from the needle during the droplet's interaction with the swirl flow airstream.

For shadowgraphy, a high-speed camera (model, Phantom VEO 640L; make, Vision Research, USA) with a Nikkor lens with a focal length of 135 mm and a minimum aperture of $f/2$ is employed. It is designated as high-speed camera 1 in the schematic diagram (figure 1). The high-speed camera 1 is positioned at $x = 180$ mm while maintaining an angle of -30° with the x axis. To illuminate the background uniformly, a high-power light-emitting diode (model, MultiLED QT; make, GSVITEC, Germany) is used along with a diffuser sheet, as shown in figure 1. The images captured using the high-speed camera 1 have a resolution of 2048×1600 pixels, and they are recorded at 1800 frames per second (f.p.s.) with an exposure duration of 1 μs and a spatial resolution of $29.88\,\mu m\,pixel^{-1}$. The droplet's image sequence is stored in the internal memory of the camera and then transferred to a computer for further processing.

The digital in-line holography set-up consists of a laser, spatial filter, collimating lenses and the high-speed camera 2 (model, Phantom VEO 640L; make, Vision Research, USA)

with a Tokina lens (focal length of 100 mm and a maximum aperture $f/2.8$; model, AT-X M100 PRO D Macro). The high-speed camera 2 is positioned at $x = 180$ mm, as shown in figure 1. A laser beam is generated using a continuous wave laser (model, SDL-532-100 T; make, Shanghai Dream Lasers Technology Co. Ltd.) that produces 100 mW of output power at a wavelength of 532 nm. The laser beam is passed through a spatial filter to produce a clean beam. The spatial filter consists of an infinity-corrected plan achromatic objective (20× magnification; make, Holmarc Opto-Mechatronics Ltd.) and a 15 µm pin-hole. The beam from the spatial filter is expanded using a plano–concave lens and then collimated using a plano–convex lens (make, Holmarc Opto-Mechatronics Ltd.) before it illuminates the droplet field of view. The diameter of the collimated beam is 50 mm. The interference patterns created due to the droplet's disintegration are recorded using the high-speed camera 2 with a resolution of 2048 × 1600 pixels at 1800 f.p.s., at an exposure duration of 1 µs and a spatial resolution of 19.27 µm pixel^{-1}. The high-speed camera 1 (used for the shadowgraphy) and high-speed camera 2 (employed for the digital in-line holography) are synchronized using a digital delay generator (model, 610036; make, TSI, USA). While presenting the results of droplet size distributions, the error bars display the standard deviation of three repetitions for each set of parameters.

2.1. *Digital in-line holography technique*

Digital in-line holography uses a collimated, coherent and expanded laser beam. The first step in digital holography is to record the interference patterns created by the scattered light from the droplets (object wave) and the unscattered background illumination (reference wave) on a camera sensor. Therefore, the recorded hologram contains both the amplitude and phase information of the object wave. The second step deals with the reconstruction of the hologram. The hologram is numerically illuminated in the reconstruction process with a reference beam to obtain droplet information at different depths. In in-line holography, the single beam acts as both a reference and an object beam.

Figure 2 illustrates the various steps involved in the pre and post-processing of the hologram recorded using digital in-line holography. The processing method consists of three major steps: (i) holographic reconstruction; (ii) network training; and (iii) post-processing of the holograms. As a first step, the background image is subtracted from the recorded holograms (see figure 3), followed by an intensity normalization process to remove noise and correct uneven illumination. The intensity normalization is represented as

$$I_N(x, y) = \frac{I - I_{min}}{I_{max} - I_{min}}, \tag{2.3}$$

where I_N is the normalized image, and I_{max} and I_{min} are the maximum and the minimum intensities of the image. A set of 30 holograms without the particle field are recorded before the start of every experiment, which is then averaged to get the mean intensity image of the background. Once the holograms are pre-processed, to obtain the 3-D optical field, the numerical reconstruction is performed using the Rayleigh–Sommerfeld equation, which is given by

$$I_r(x, y, z) = I_h(y, z) \otimes h(x, y, z), \tag{2.4}$$

where $I_r(x, y, z)$ is the 3-D complex optical field obtained from reconstruction. The term $I_h(y, z)$ represents the pre-processed hologram, $\otimes$ denotes the convolution operation and $h(x, y, z)$ is the diffraction kernel. The Rayleigh–Sommerfeld diffraction kernel in the

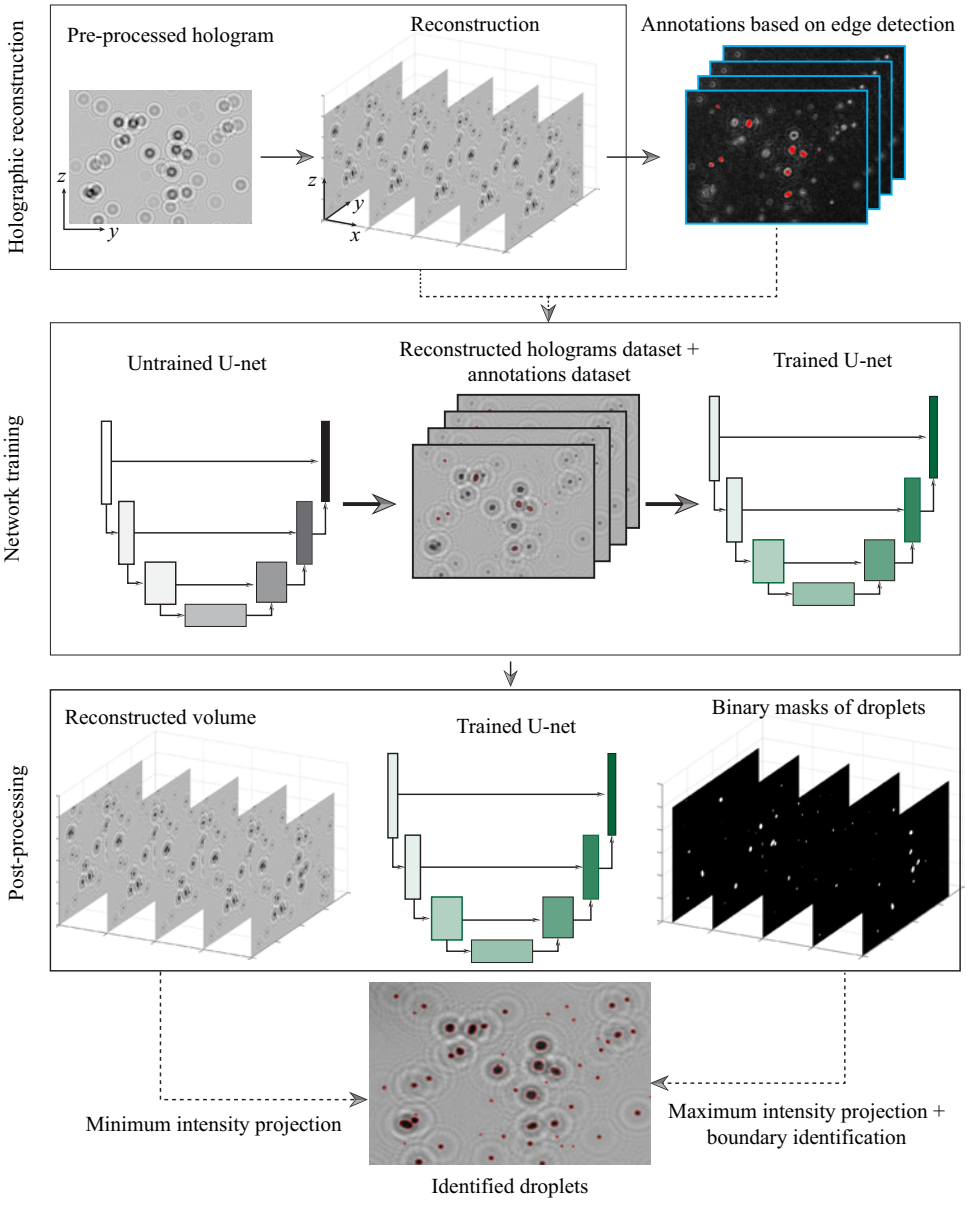

Figure 2. Various steps of the digital in-line holography technique employed in the present study.

frequency domain can be expressed as (Katz & Sheng 2010)

$$H(f_x, f_y, z) = \exp\left(jkz\sqrt{1 - \lambda^2 f_x^2 - \lambda^2 f_y^2}\right), \tag{2.5}$$

where $j = \sqrt{-1}$ and $k = 2\pi/\lambda$ represents the wavenumber; λ is the wavelength of the incident beam. The spatial frequency in the x and y directions are expressed by f_x and f_y, respectively. In the frequency domain, using the convolution theorem, the complex optical field (3-D image of objects), I_r can be evaluated as

$$I_r(x, y, z) = \mathrm{FFT}^{-1}\left\{\mathrm{FFT}\left[I_h(y, z)\right] \times H(f_x, f_y, z)\right\}. \tag{2.6}$$

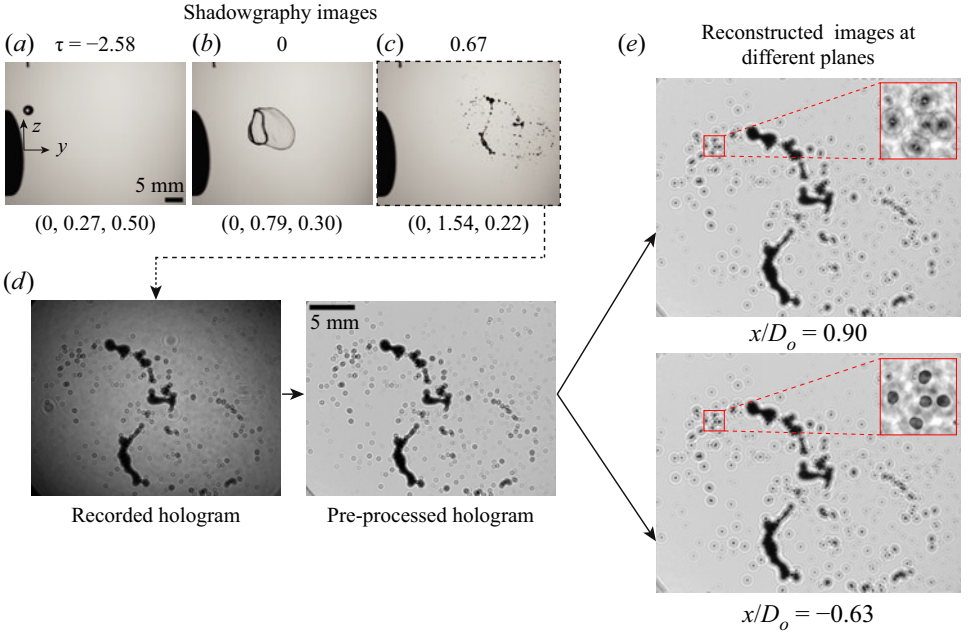

Figure 3. A demonstration of different steps to obtain the droplet size distribution after breakup using the in-line holography technique. (*a–c*) Temporal evolution of the bag formation and breakup obtained using the shadowgraphy technique. The dimensionless coordinates of the droplet $(x/D_0, y/D_0, z/D_0)$ are mentioned at the bottom of the shadowgraphy images at different instants. Outlet of the nozzle and the tip of the dispensing needle are indicated in the left and top of the shadowgraphy images. (*d*) Image at $\tau = 0.67$ is considered to reconstruct the hologram at different planes in the x direction (panel (*e*)). Here, $We = 14.53$, $Sw = 0$ and $(x_d/D_o, y_d/D_o, z_d/D_o) = (0.0, 0.27, 0.95)$. An animation showing the different holography reconstructed planes at $\tau = 0.67$ is provided as supplementary movie 1.

Here, FFT represents the fast Fourier transform operator. The in-plane intensity information is obtained from the magnitude of the complex optical field in the corresponding plane. The reconstruction is performed in a series of planes with spacing $\Delta x = 100\,\mu$m across the test volume centred at the nozzle axis. The dimensions of the reconstructed volume are 45 mm along the x direction (along the optical axis), 40 mm along the y direction and 31.3 mm along the z direction. The spatial resolutions for the shadowgraphy and holography images are $29.88\,\mu\text{m pixels}^{-1}$ and $19.2\,\mu\text{m pixels}^{-1}$, respectively. They are calibrated using a calibration target (TSI Inc).

Figure 3 shows a typical bag fragmentation of a water droplet under a straight airstream without swirl ($Sw = 0$) for $We = 14.53$. In this case, the dispensing needle is located at $(x_d/D_o, y_d/D_o, z_d/D_o) = (0.0, 0.27, 0.95)$. The temporal evolution of the fragmentation phenomenon obtained from shadowgraphy is shown in figure 3(*a–c*). It can be seen that the droplet enters the potential core region of the straight airstream at $\tau = -2.58$ and bulges to develop a bag of maximum size at the onset of its breakup at $\tau = 0$. At $\tau = 0.67$, bag and rim fragment into satellite droplets. At this instant, we illustrate the volume reconstruction, including the sample hologram (shown in figure 3(*d*)) and the reconstructed images at two different depths along the x direction, as shown in figure 3(*e*). The reconstructed images at $x/D_0 = 0.9$ and -0.63 in figure 3(*e*) highlight the in-focus images of the satellite droplets at different depths.

The second step (see figure 2) in holographic processing consists of training a convolution neural network for segmenting the droplet images. A number of methods have

been developed in the literature to determine the position and shape of droplets within the 3-D reconstructed volume. For example, the droplet position and morphology are evaluated based on maximum edge sharpness and maximum intensity minimization (Gao *et al.* 2013*a*,*b*; Guildenbecher *et al.* 2013). The common practice is to use edge detection followed by intensity thresholding to demarcate droplet boundaries in the images. Due to the unwanted noise surrounding the droplets region, conventional image processing techniques based on intensity gradients cannot fully segment the droplets. Additionally, if the concentration of droplets is dense, segmenting them based on traditional image processing techniques becomes difficult. To overcome the above-mentioned difficulties and to accurately discern the boundaries of droplets, the images are segmented using a 2-D convolutional neural network based on the U-Net architecture (Ronneberger, Fischer & Brox 2015; Falk *et al.* 2019). The U-Net is a semantic segmentation method that was initially developed for analysing biological images (Falk *et al.* 2019; Ibtehaz & Rahman 2020). As part of its implementation, U-Net employs two paths for pixel-level classification and localization. By employing a series of convolutional and max-pooling layers, the first path captures image context and the second path is an expanding path for detecting precise localization. Additionally, the data augmentation is implemented by elastically deforming the annotated input images. This allows the network to make better use of existing annotated data. An extensive discussion on the network architecture and its functionality can be found in the seminal work by Ronneberger *et al.* (2015). In the present study, a total of 50 manually annotated (ground truth) images from the reconstructed volume are used to train the network. The ground truth annotation is performed using local thresholding around each satellite droplet. The set of manually annotated images from various cases enables the use of a single set of training weights for all experiments. Prior to the training, the current method (Falk *et al.* 2019) performs data augmentation by rigidly and elastically deforming the ground truth images to eliminate the need for large datasets. The manual annotations or masks are created based on edge sharpness maximization. As annotating the entire image manually is difficult, only subzones of images are manually labelled and used for training. A GPU-based open-source software developed by Ronneberger *et al.* (2015) is used for training the network. On an NVIDIA P2200 GPU, training the network takes approximately 12 h.

The final step involves the post-processing of the 3-D reconstructed volume to determine the droplet boundaries. The trained network is applied to every plane of the reconstructed 3-D volume, as shown in figure 2. The network's output directly provides the binary masks corresponding to the droplet boundaries in each plane. The final processing involves the maximum intensity projection of the binary mask, elimination of droplets smaller than 3 pixels (Berg 2022) and estimation of the equivalent diameter. The network validation using synthetic holograms and the associated errors are provided in the supplementary material (figure S3).

To validate the results obtained from our analysis, we compare the size distribution of satellite droplets resulting from the fragmentation of a water droplet under a straight airstream (without swirl) in a cross-flow configuration with that reported by Guildenbecher *et al.* (2017). It is to be noted that we consider a water droplet of $d_0 = 3.09$ mm ($We = 14.53$) while Guildenbecher *et al.* (2017) used an ethanol droplet of $d_0 = 2.54$ mm ($We = 13.8$). The properties of both water and ethanol are listed in table 1. Figure 4 depicts the comparison of the variation of the normalized mean diameter (d_{10}/d_0) with normalized time ($t/(\mu^3/\sigma^2\rho)$). In this figure, we have adopted a normalization for time based on fluid properties to compare the results associated with different working fluids considered in our experiments (water) and by Guildenbecher *et al.* (2017) (ethanol). Here, d_{10} is a

Fluids	Density, ρ (kg m^{-3})	Viscosity, μ (mPa s)	Surface tension, σ (mN m^{-1})
Water	998	1.0	72.8
Ethanol	789	1.2	24.4

Table 1. Fluid properties of water and ethanol used in the present study and considered by Guildenbecher *et al.* (2017), respectively.

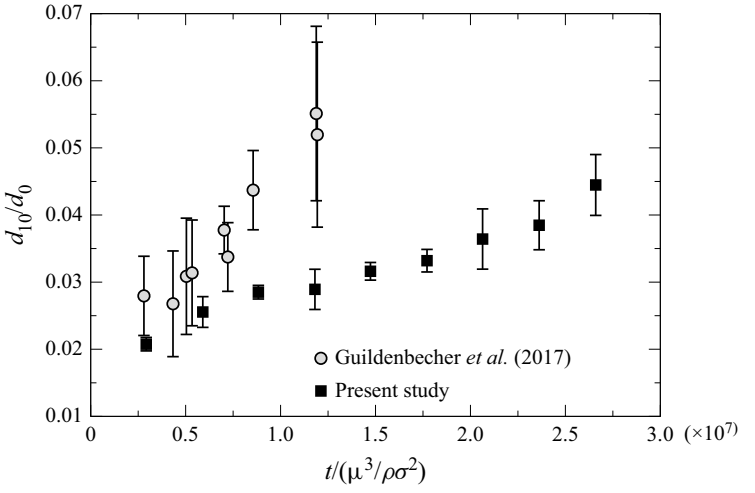

Figure 4. Comparison of the temporal variation of normalized mean diameter (d_{10}/d_0) obtained from our experiments with that of Guildenbecher *et al.* (2017). In the present study, a water droplet of $d_0 = 3.09$ mm ($We = 14.53$) is used, while Guildenbecher *et al.* (2017) considered an ethanol droplet of $d_0 = 2.54$ mm ($We = 13.8$). In our experiments, the error bar represents the standard deviation obtained from the three repetitions. The uncertainty bar for the data of Guildenbecher *et al.* (2017) corresponds to the standard deviation from forty-four realizations.

number-based spatial average of the diameters of all droplets and is given by

$$d_{10} = \int_0^\infty \mathrm{d}p(d)\,\mathrm{d}d, \tag{2.7}$$

where $p(d)$ is the probability density function of the diameters of the satellite droplets. We calculate d_{10} from the number-based-average of satellite droplets. It can be seen in figure 4 that at early times, the ratio d_{10}/d_0 is small due to the rupture of the bag near its tip. The fragmentation of the rim and nodes occurs at later stages, providing several larger satellite droplets. This results in all the droplets contributing to the estimation of d_{10}, increasing the normalized mean diameter of the satellite droplets, d_{10}/d_0. It can also be observed that at initial times, the estimated d_{10}/d_0 from the present experiment is in reasonable agreement with that of Guildenbecher *et al.* (2017). However, the results differ at the later stages of fragmentation. It is to be noted that the total breakup time of the water droplet in our experiments compares well with that of Kulkarni & Sojka (2014). Quantitatively, the total breakup time obtained in our experiment is 4.44 ms, while it is 6 ms in the experiment of Kulkarni & Sojka (2014). The Rayleigh–Taylor instability develops as a result of the penetration of the air phase into the liquid phase, which causes the fragmentation of

the liquid droplet. The Atwood number, $At = (\rho - \rho_a)/(\rho + \rho_a)$, for the water–air and ethanol–air systems are 1.2 and 0.997, respectively. As a result, one would expect a more substantial Rayleigh–Taylor instability to be developed in the case of the water–air system, as considered in our study, than the ethanol–air system considered by Guildenbecher *et al.* (2017). This, in turn, helps a water droplet to fragment into smaller satellite droplets more easily than an ethanol droplet. Thus, it can be observed in figure 4 that the normalized mean diameter of the satellite droplets in our experiment (water droplet) is smaller than that reported by Guildenbecher *et al.* (2017) for an ethanol droplet. The difference in fluid properties of the liquids considered in our experiment and by Guildenbecher *et al.* (2017) may not significantly affect the rupture of the thin film of the bag but mainly influences the fragmentation of the rim breakup phenomenon. While the rupture of the bag is due to the pressure difference across its interface caused by the aerodynamic force, the later stage of rim fragmentation is driven by the capillary Rayleigh–Plateau instability (Jackiw & Ashgriz 2021). The values of the Ohnesorge number, $Oh = \mu/\sqrt{\rho\sigma d_0}$, in our case and in the study of Guildenbecher *et al.* (2017) are approximately 0.002 and 0.005, respectively. Therefore, at the later stage, the rim fragmentation in our study is slower than that reported in the work of Guildenbecher *et al.* (2017).

3. Results and discussion

As discussed in § 1, Kirar *et al.* (2022) employed shadowgraphy to illustrate different breakup modes for an ethanol droplet of diameter $d_0 = 2.7 \pm 0.07$ mm and discovered a new breakup mode (retracting bag breakup mode) for a low value of the swirl number (Sw). To the best of our knowledge, the study by Kirar *et al.* (2022) is the first to explore the phenomenon of droplet breakup in a swirling airstream. In contrast to the present study, which focuses on droplet size distribution, their aim was to demonstrate a new breakup mode in a swirling flow using Raleigh–Taylor instability. Thus, before discussing the size distribution of droplets obtained using the digital in-line holography technique, we begin the presentation of our results by demonstrating the temporal evolution of the morphologies of a freely falling water droplet of diameter $d_0 = 3.09 \pm 0.07$ mm interacting with an airstream of different swirl strengths. Figure 5 depicts the temporal evolution of the droplet morphology for the no-swirl ($Sw = 0$), low-swirl ($Sw = 0.47$) and high-swirl ($Sw = 0.82$) conditions for a fixed value of the Weber number ($We = 12.1$). The dimensionless locations of the tip of the dispensing needle ($x_d/D_o, y_d/D_o, z_d/D_o$) are (0.0, 0.01, 0.80), (0.12, 0.01, 0.80) and (0.12, 0.01, 0.80) for $Sw = 0$, 0.47 and 0.82, respectively. In the no-swirl case, the droplet is dispensed at the axis of symmetry, $x_d/D_o = 0$, but in swirl flow cases, the droplet is dispensed at $x_d/D_o = 0.12$, so that the droplet interacts with the swirl airstream in oppose/cross-flow conditions. The location of the dispensing needle for the no-swirl and swirl cases is shown in figure S2 of the supplementary material. These locations are chosen in accordance with the regime map presented by Kirar *et al.* (2022) (see figure S4 in the supplementary material). The dimensionless time, $\tau (\equiv t/t_d)$, is mentioned at the top of each panel in figure 5. Here t is the physical time and $t_d = d_0\sqrt{\rho/\rho_a}/U$ is the characteristic deformation time. In our experiments, $\tau = 0$ represents the onset of the breakup of the droplet. In the case of the bag breakup mode, it is the instant the inflated bag ruptures, but in the case of the vibrational breakup mode, it is the instant the droplet starts to break into smaller droplets of comparable size. Thus, the value of τ before the fragmentation instant is a negative number.

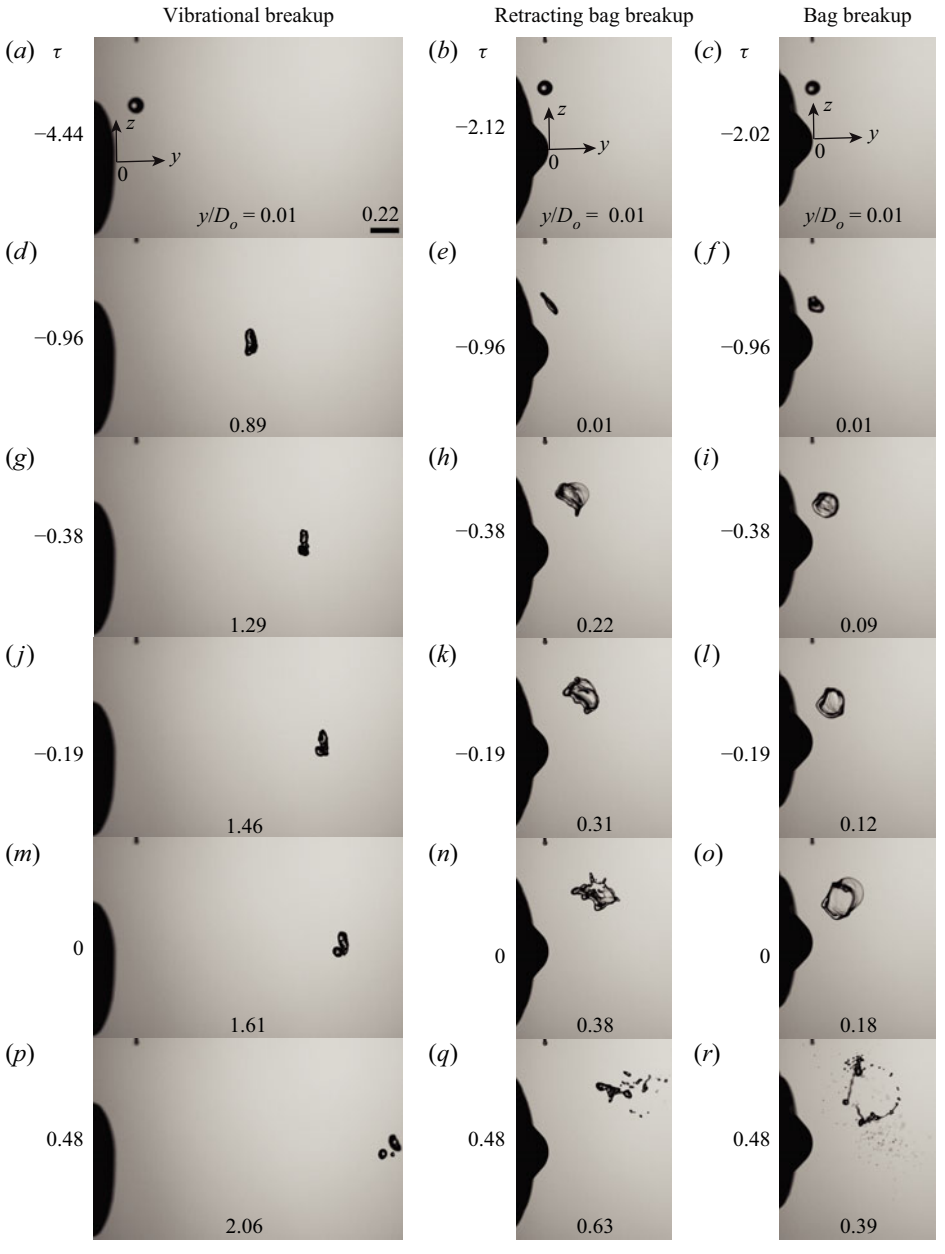

Figure 5. Effect of the swirl number, Sw, on the fragmentation process of a water droplet (obtained from shadowgraphy) for $We = 12.1$. (*a*,*d*,*g*,*j*,*m*,*p*) $Sw = 0$ (vibrational breakup), (*b*,*e*,*h*,*k*,*n*,*q*) $Sw = 0.47$ (retracting bag breakup) and (*c*,*f*,*i*,*l*,*o*,*r*) $Sw = 0.82$ (normal bag breakup). The value of τ is indicated in each panel. The dimensionless scale-bar is shown in panel (*a*). The dimensionless location $(x_d/D_o, y_d/D_o, z_d/D_o)$ of the dispensing needle for $Sw = 0$, 0.47 and 0.82 are (0.0, 0.01, 0.80), (0.12, 0.01, 0.80) and (0.12, 0.01, 0.80), respectively. To show the migration due to the airstream, the dimensionless position of the droplet in the flow direction, y/D_0, is mentioned at the bottom of each panel. Kirar *et al.* (2022) have shown similar breakup modes for an ethanol droplet. The droplet breakup phenomena for $Sw = 0$, 0.47 and 0.82 are provided as supplementary movies 2–4, respectively.

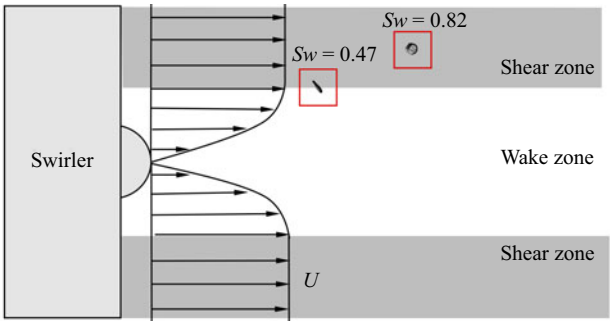

Figure 6. Schematic of the core-annular flow field of the high shear and wake zones created due to the swirling effect. The droplets during their interaction with the swirl airstream for low and high swirl strengths are also depicted.

It can be seen in figure 5(*a*,*d*,*g*,*j*,*m*,*p*) that the droplet undergoes a vibrational breakup mode in the no-swirl case, but it exhibits a retracting bag breakup mode for $Sw = 0.47$ (figure 5*b*,*e*,*h*,*k*,*n*,*q*) and a normal bag breakup mode for $Sw = 0.82$ (figure 5*c*,*f*,*i*,*l*,*o*,*r*). In the no-swirl case, as the spherical droplet enters the aerodynamic field, it deforms into a thick disk ($\tau = -0.96$) as a result of asymmetrical pressure distribution at the front and rear of the droplet. At this stage, the surface tension force opposes further deformation and tries to make the droplet have a spherical shape. Consequently, the droplet oscillates with an increasing amplitude due to the competition between the aerodynamic force favouring the deformation, and the viscous and surface tension forces opposing it (at $\tau = -0.38$ and -0.19). As the oscillations reach an amplitude comparable to the drop's radius, it fragments into smaller satellite droplets.

For the low swirl strength ($Sw = 0.47$), the droplet quickly changes its shape from a sphere to a slightly tilted disk due to the aerodynamic force in the direction of vane inclination. As the swirl is not strong enough, only the bottom part of the disk enters the low-velocity zone (schematically shown in figure 6) generated by the wake of the swirler. Consequently, the rest of the disk, which is in the high-shear region, undergoes inflation to form a bag. In the high-shear zone, a negative pressure gets created that retracts the bag sheet in a direction opposite to the direction of bag growth ($\tau = -0.19$). Subsequent retraction of the bag exhibits capillary instability and causes the bag to rupture ($\tau = 0$). When the bag ruptures, the surface tension pulls the liquid film surrounding it to the rim, causing it to break into satellite droplets ($\tau = 0.48$).

For the high swirl strength ($Sw = 0.82$), the droplet rapidly changes its topology from a sphere to a disk shape due to the unequal pressure distribution around its periphery ($\tau = -2.02$ to -0.96). The lower portion of the disk tilts as it is exposed to an opposed flow condition. In this case, the swirling strength is sufficient to retain the disk in the shear zone. In other words, the high-swirl flow does not allow the disk to enter into the low-velocity zone created by the wake of the swirler (see figure 6). As a result, the entire disk adjusts vertically, making the breakup process more efficient ($\tau = -0.38$ to -0.19). The middle of the disk elongates, generating a thin liquid sheet in the centre and a thick rim on the outside ($\tau = 0$). Finally, high shear velocity causes the bag and rim to break in the shear zone ($\tau = 0.48$).

Next, we investigate the size distribution of a droplet after fragmentation under different swirl air strengths. Figure 5 demonstrates that the droplet disintegrates into a few large satellite droplets in the no-swirl situation for $We = 12.1$ due to the vibrational breakup. Therefore, in the following, we mainly focus on the size distribution at the low and

high swirl strengths that encounter retracting bag and normal bag breaking events. Figure 7 depicts the temporal evolution of the droplet size distribution for $Sw = 0.47$ (low swirl strength) at $We = 12.1$. In figure 7, the first, second and third columns show the shadowgraphy images, holograms and the resultant size distributions of droplets at different instants, respectively. At $\tau = 0$, the retracted bag ruptures due to the negative pressure gradient created by the wake of the swirler. It is interesting to note that although the bag is ruptured, it does not produce any satellite drops at this stage ($\tau = 0$). This phenomenon is distinct from the normal bag breakup observed in a straight airstream at high Weber numbers (see, for instance, Guildenbecher *et al.* 2009; Kulkarni & Sojka 2014; Soni *et al.* 2020). For $\tau > 0$, it can be seen in figure 7 that the bag sheet continues to retract and finally impinges on the rim. This leads to the fragmentation of the upper portion of the rim due to the capillary Rayleigh–Plateau instability. The fragmentation of the rim continues which leads to the generation of smaller secondary droplets of diameter up to 300 μm, as indicated by the histogram at $\tau = 0.37$ in figure 7(*h*). During this process, the nodes formed on the rim due to the Rayleigh–Taylor instability also disintegrate, and this process continues until $\tau = 0.56$ thereby producing more droplets in a broader size range, $300\,\mu\text{m} < d < 1200\,\mu\text{m}$. Finally, as the bottom of the disk is entrapped in the wake zone, it creates a low aerodynamic force that leads to thicker nodes. These thicker nodes (at $\tau = 0.75$) break eventually because of the continuous swirl airflow, which in turn, creates larger satellite droplets ($d > 1200\,\mu\text{m}$). Note that the histogram is truncated at $d \approx 1600\,\mu\text{m}$, and the distribution of larger droplets is not shown here. A volume-weighted distribution presented later in figure 11 provides the entire size distribution of the droplets.

Figure 8 illustrates the temporal evolution of the droplet size distribution for $Sw = 0.82$ (high swirl strength) for the same Weber number ($We = 12.1$). In this case, the entire liquid bulk exposes to the shear zone (see the droplet position in figure 6) and changes its morphology from a disk to a thick toroidal rim with an elongated bag ($\tau = 0$). The bursting of this bag ($\tau = 0.18$) generates very fine satellite droplets ($d < 300\,\mu\text{m}$). Subsequently, the remaining portion of the bag liquid sheet propagates back towards the rim due to unbalanced tension and is finally absorbed in the rim. At this stage ($\tau = 0.38$), the number of tiny satellite droplet increases and fragmentation of the rim initiates. The breakup of the rim advances and results in generation of intermediate-sized droplets ($300\,\mu\text{m} < d < 900\,\mu\text{m}$) at $\tau = 0.48$. Finally, due to the Rayleigh–Taylor instability, the nodes on the rim disintegrate and produce bigger satellite droplets ($d > 900\,\mu\text{m}$) at $\tau = 0.66$. At this stage, the coalescence of smaller droplets also contributes to the size distribution.

Figure 9(*a*) shows temporal variation of normalized number-mean diameter for different swirl numbers at $We = 12.1$. The error bar at each data point represents the standard deviation of three repetitions. As time progresses, the relative velocity between airflow and liquid bulk decreases, thus producing bigger droplets leading to an increase in the number-mean diameter of satellite droplets. As discussed earlier, while the low-swirl case ($Sw = 0.47$) produces larger size droplets due to the fragmentation of rim and nodes (bag-film breakup does not contribute to the size distribution), in the high-swirl case ($Sw = 0.82$), the breakup of the bag, rim and nodes contribute to the number-mean diameter and thereby producing smaller satellite droplets.

The Sauter mean diameter (commonly termed as SMD or d_{32}) is defined as the surface area moment mean, which provides the mean size of a given droplet distribution. Thus, the reciprocal of the Sauter mean diameter is a direct measure of the surface area per unit

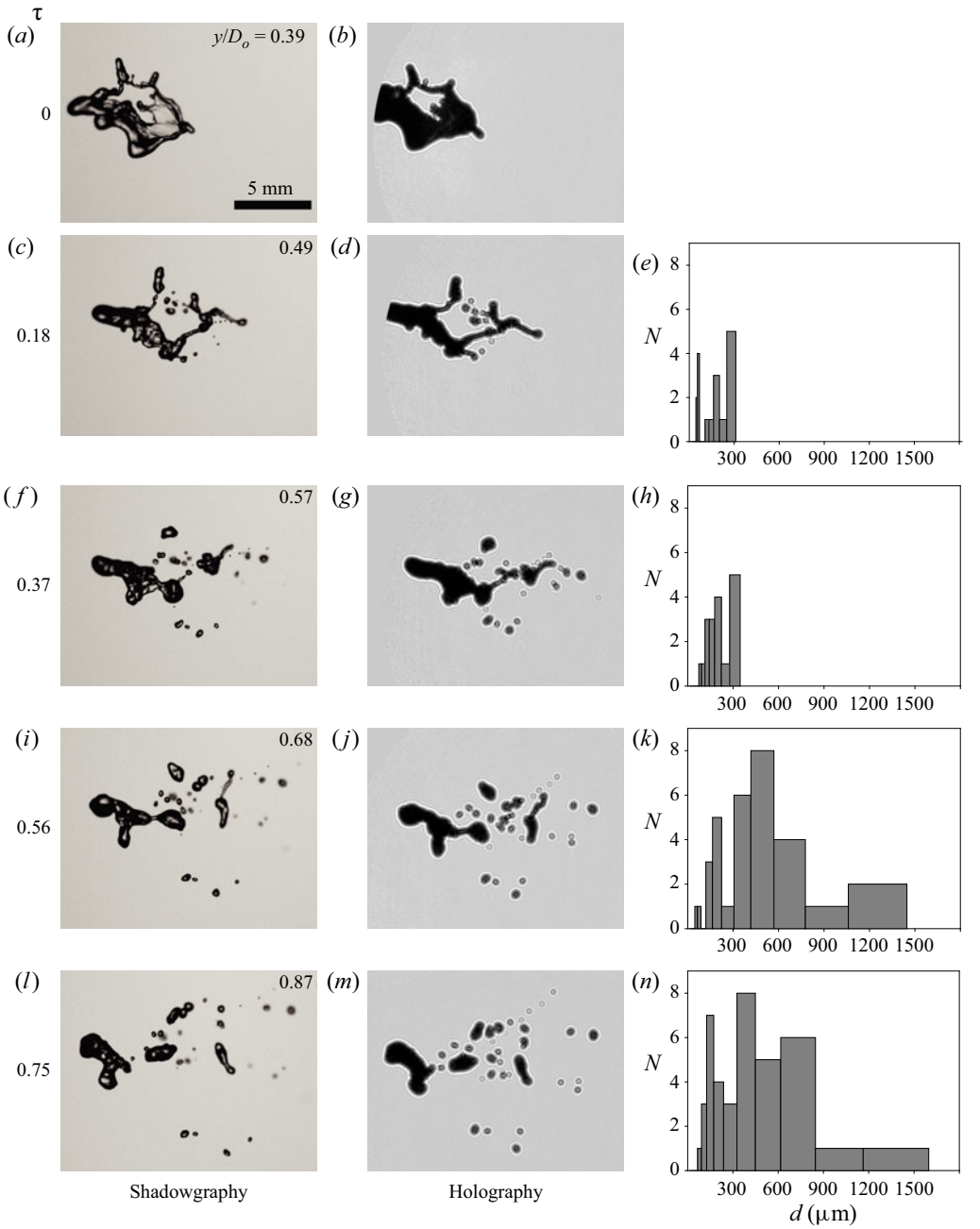

Figure 7. Temporal evolution of the droplet size distribution for $Sw = 0.47$ and $We = 12.1$. Panels (*a*,*c*,*f*,*i*,*l*) and (*b*,*d*,*g*,*j*,*m*) represent the shadowgraphy images and recorded holograms obtained using the in-line holography. The values of the dimensionless time, τ, are mentioned on the left-hand side of panels (*a*,*c*,*f*,*i*,*l*) measured from the instant at the onset of breakup. The scale-bar is shown in panel (*a*). Panels (*e*,*h*,*k*,*n*) depict the histograms of the droplet size distribution (the droplet counts, N versus the droplet diameter, d) at different instants after the breakup. The dimensionless location of the dispensing needle is at $(x_d/D_o, y_d/D_o, z_d/D_o) = (0.12, 0.01, 0.80)$. The dimensionless position of the droplet in the flow direction, y/D_0, is mentioned at the top-right corner of each panel of the shadowgraphy images.

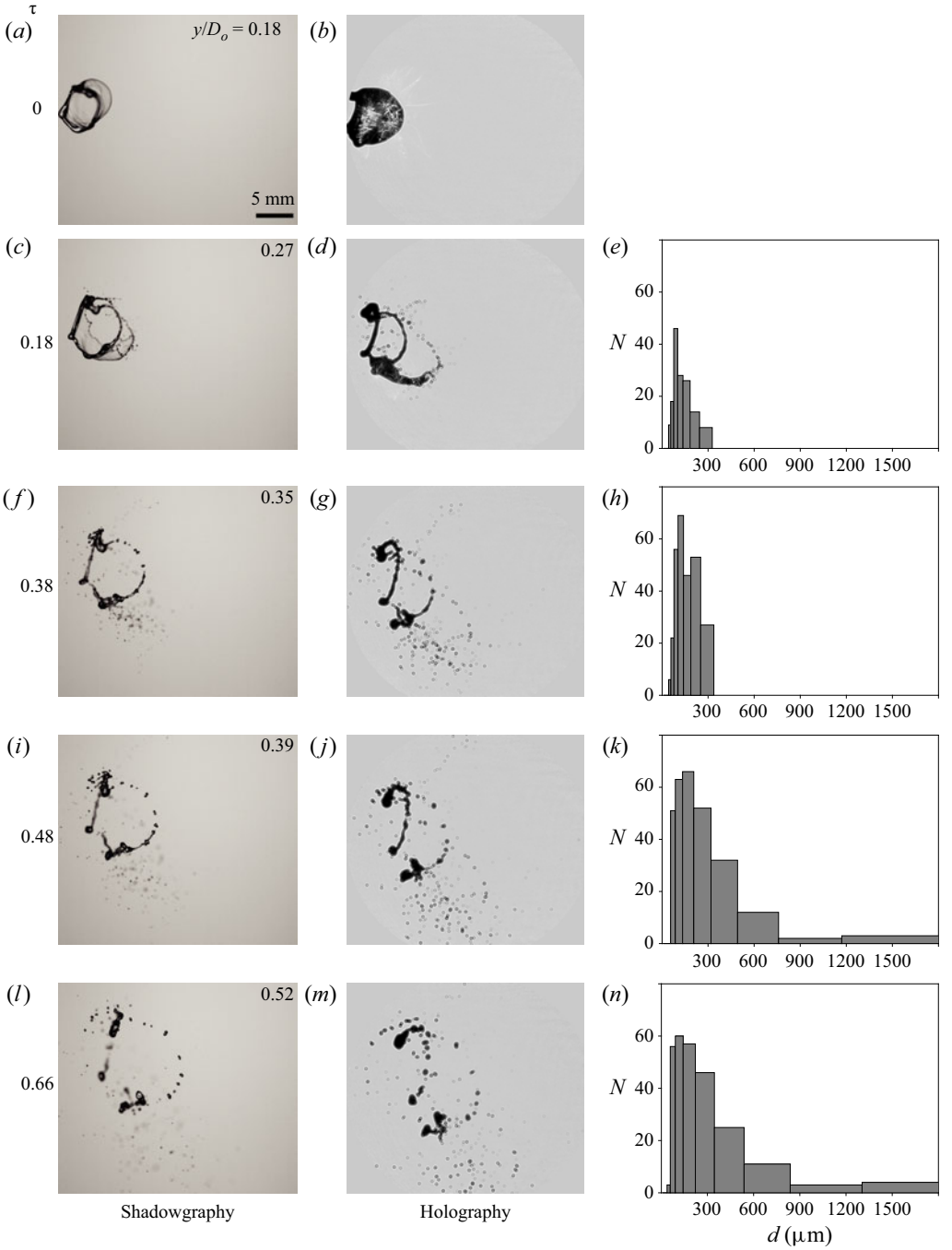

Figure 8. Temporal evolution of the droplet size distribution for $Sw = 0.82$ and $We = 12.1$. Panels (a,c,f,i,l) and (b,d,g,j,m) represent the shadowgraphy and the holography (recorded hologram) images, respectively. The values of the dimensionless time, τ are mentioned on the left-hand side of (a,c,f,i,l) measured from the instant at the onset of breakup. The scale-bar is shown in panel (a). Panels (e,h,k,n) depicts the histogram of the droplet size distribution (the droplet counts, N, versus the droplet diameter, d) at different instants after breakup. The dimensionless location of the dispensing needle is $(x_d/D_o, y_d/D_o, z_d/D_o) = (0.12, 0.01, 0.80)$. The dimensionless position of the droplet in the flow direction, y/D_0, is mentioned at the top-right corner of each panel of the shadowgraphy images.

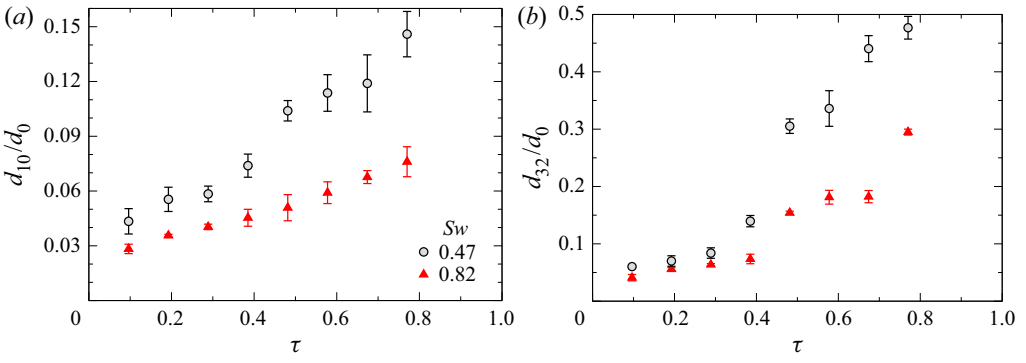

Figure 9. Temporal variation of normalized mean diameters (*a*) (d_{10}/d_0) and (*b*) (d_{32}/d_0) for different swirl numbers at $We = 12.1$.

volume of the satellite droplets, which is given by

$$d_{32} = \frac{\int_0^\infty d^3 p(d)\,\mathrm{d}d}{\int_0^\infty d^2 p(d)\,\mathrm{d}d}. \tag{3.1}$$

In the present study, we use the ratio between the mean volume and mean surface area of the satellite droplets to calculate d_{32}.

To get a better insight into the size distribution of satellite droplets, we plot the temporal variation of normalized Sauter mean diameter (d_{32}/d_0) for different swirl numbers in figure 9(*b*). It can be seen that the Sauter mean diameter increases with time for both the low and high swirl strengths. However, in comparison to low swirl strength, high swirl strength produces secondary droplets with a smaller value of d_{32}. Therefore, for the same aerodynamic force, the high swirl strength generates more surface area (and hence more surface energy) than the low swirl strength after fragmentation. At a later time ($\tau = 0.5$), the sudden jumps in the variation of d_{32}/d_0 is associated with the increase in the number of larger droplets.

3.1. *Prediction of droplet size distribution from statistical theory*

In this section, we compare our experimentally determined droplet size distribution in swirl airstreams with an existing theoretical model, which was initially developed for the no-swirl conditions (Villermaux & Bossa 2009). According to Villermaux & Bossa (2009), the corrugated rims contribute to the overall size distribution, regardless of the mode of breakup (whether it is a bag breakup or a direct transition from drop to ligament). In a strong shear flow, the detached ligament from the corrugated rim elongates and disintegrates into numerous blobs due to capillary instability. Marmottant & Villermaux (2004) remarked that during this phase, the blobs of various shapes and sizes also coalesce, leading to the formation of larger droplets because of the Laplace pressure difference. Therefore, the resultant droplets have a diameter greater than the thickness of the ligament. All these processes are known to affect the overall size distribution that follows a single parameter gamma distribution function (Villermaux 2007) as

$$P_b = \frac{\nu^\nu}{\Gamma(\nu)} \left(\frac{d}{d_1}\right)^{\nu-1} e^{-\nu(d/d_1)}, \tag{3.2}$$

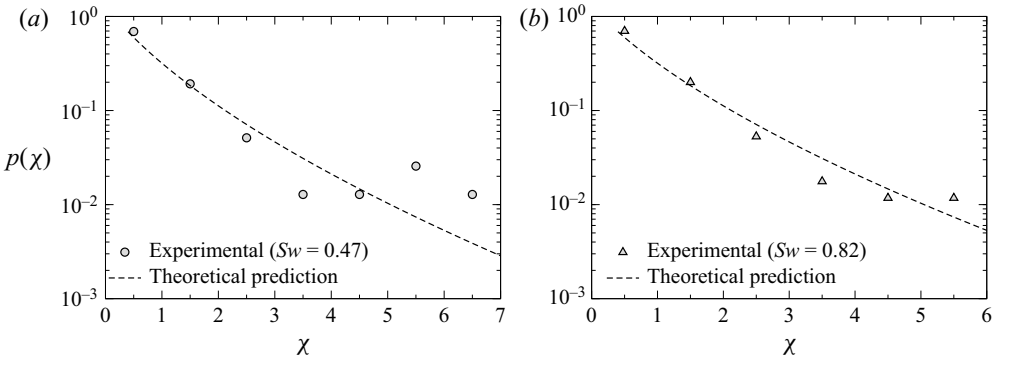

Figure 10. Comparison of the variation of $p(\chi)$ versus $\chi(d/\langle d\rangle)$ obtained from our experiments with the theoretical prediction from (3.4) (Villermaux & Bossa 2009) for (*a*) $Sw = 0.47$ at $\tau = 0.75$ and (*b*) $Sw = 0.82$ at $\tau = 0.66$. The rest of the parameters are the same as those in figure 7.

where $\nu = 1/(\gamma - 1)$ reflects the regularity of the initial shape of the ligament, wherein γ is the interaction parameter and d_1 is the average blob diameter. For a corrugated ligament, $\gamma > 1$ that induces a skewed broader distribution of sizes with an exponential tail. Its value approaches to 1 as the ligament is smoother. Thus, the value of ν increases with the smoothness of the ligament, which in turn give rise to a uniform distribution of drop sizes. The gamma distribution closely fits with the present experiments when the value of $\gamma = 1.25$. The larger droplets are distributed exponentially in the distribution shown above. There is a high likelihood that these droplets will keep disintegrating until they stabilize. Due to the consecutive breaking up of large droplets, the total size distribution that results from this follows an exponential distribution as (Villermaux & Bossa 2009)

$$P(d) = \int P_b \frac{e^{-d_1/\langle d\rangle}}{\langle d\rangle}\,\mathrm{d}d_1, \tag{3.3}$$

where $P(d)$ is the number probability density. Thus, the dimensionless number probability density, $p(\chi) = \langle d\rangle P(d)$, is giving by

$$p(\chi) = \frac{32}{3}\chi^{3/2}\mathrm{K}_3(4\sqrt{\chi}), \tag{3.4}$$

where K_3 represents the Bessel function of third order, $\langle d\rangle$ denotes the average drop size and $\chi = d/\langle d\rangle$.

Figure 10(*a*,*b*) depicts the comparison of dimensionless number probability density, $p(\chi)$ obtained from our experiments with the theoretical prediction (3.4) for the low swirl ($Sw = 0.47$) and high swirl ($Sw = 0.82$) strengths, respectively. For both cases, a typical instant is chosen when the fragmentation ceases. It can be observed in figure 10(*a*) that for low swirl strength ($Sw = 0.47$) that exhibits retracting bag type breakup, the theoretical prediction agrees with the experimental observation for small droplets ($\chi < 3$), but deviates from the experimental results for large droplets. As discussed earlier, in the case of retracting bag breakup, the lower portion of the disk/rim is entrapped in the wake zone of the swirler and does not participate in the bag formation process. This results in producing larger droplets and alters the size distribution as observed for $\chi > 3$ in figure 10(*a*). Additionally, the rim instability and subsequent droplet count may be impacted by the bag's retraction and impingement on the rim. This phenomenon is entirely missing in the event of a normal bag breakup. This is evident in figure 10(*b*) for

$Sw = 0.82$ that undergoes a normal bag breakup and shows a better agreement with the theoretical prediction. However, a close inspection reveals that the theoretical prediction differs slightly from the experimental results for very large droplets ($\chi > 3$). It is due to the fact that all breakup modes are not taken into consideration in theoretical prediction (Villermaux & Bossa 2009).

3.2. *Multi-modal size distribution*

In the preceding section, we have analysed the nature of the size distribution based on the droplet counts by fitting a single parameter gamma distribution. However, the single parameter distributions cannot be used to distinguish between various mechanisms responsible for droplet breakup. Additionally, the number mean diameter is a required input parameter for this distribution. Jackiw & Ashgriz (2022) developed an analytical model to predict the combined multi-modal distribution, accounting for various mechanisms, for the aerodynamic breakup of droplets in a no-swirl condition.

In the present study, for swirl airstreams, we have followed a similar approach as that of Jackiw & Ashgriz (2022) by considering the volume-weighted probability density function, P_v, instead of the number-weighted probability density function, P_n, as the distribution based on P_n is more biased towards the smaller size droplets. The volume-weighted density refers to the ratio of the total volume of droplets of a specific diameter to the total volume of all droplets. Thus, P_v is given by

$$P_v = \frac{\zeta^3 P_n}{\displaystyle\int_0^\infty \zeta^3 P_n d\zeta} = \frac{\zeta^3 P_n}{\beta^3 \Gamma(\alpha+3)/\Gamma(\alpha)}, \tag{3.5}$$

where $\zeta (= d/d_0)$ denotes the normalized droplet size, Γ represents the gamma function, and $\alpha = (\bar{\zeta}/\sigma_s)^2$ and $\beta = \sigma_s^2/\bar{\zeta}$ are the shape and rate parameters, respectively. Here, $\bar{\zeta}$ and σ_s are the mean and standard deviation of the distribution. The expression for P_n is given by

$$P_n = \frac{\zeta^{\alpha-1} e^{-\zeta/\beta}}{\beta^\alpha \Gamma(\alpha)}. \tag{3.6}$$

In the case of bag fragmentation, three modes, namely, the node, rim and bag breakup modes, contribute to the overall size distribution of satellite droplets. Therefore, it is essential to take into account their relative contribution to the size distribution by considering the weighted summation of each mode. The total P_v determined by the weighted sum of each mode is given by

$$P_{v,Total} = w_N P_{v,N} + w_R P_{v,R} + w_B P_{v,B}, \tag{3.7}$$

where $w_N = V_N/V_0$, $w_R = V_R/V_0$ and $w_B = V_B/V_0$ represent the contributions of volume weights from the node, rim and bag, respectively. Here, V_N, V_R, V_B and V_0 are the node, rim, bag and the initial droplet volumes, respectively.

To begin with, we will elucidate the volume weight of each mode. The volume weight corresponding to the node breakup, w_N, can be estimated as

$$w_N = \frac{V_N}{V_0} = \frac{V_N}{V_D}\frac{V_D}{V_0}, \tag{3.8}$$

where V_D is the disk volume. For bag breakup, V_D/V_0 is approximately equal to unity because the entire initial volume of the drop is converted into the disk (i.e. there is no

undeformed core). The ratio V_N/V_D indicates the volume fraction of the nodes relative to the disk, which is approximately 0.4 as considered by Jackiw & Ashgriz (2022).

The volume weight of the rim, w_R, can be evaluated from the expression given by (Jackiw & Ashgriz 2021)

$$w_R = \frac{V_R}{V_0} = \frac{3\pi}{2}\left[\left(\frac{2R_i}{d_0}\right)\left(\frac{h_i}{d_0}\right)^2 - \left(\frac{h_i}{d_0}\right)^3\right], \tag{3.9}$$

where h_i denotes the disk thickness and R_i is the major radius of the rim. The value of h_i and R_i can be evaluated as (Jackiw & Ashgriz 2022)

$$\frac{h_i}{d_0} = \frac{4}{We_r + 5\left(\dfrac{2R_i}{d_0}\right) - 4\left(\dfrac{d_0}{2R_i}\right)} - \frac{1}{20}, \tag{3.10}$$

and

$$\frac{2R_i}{d_0} = 1.63 - 2.88e^{(-0.312We)}. \tag{3.11}$$

Here, $We_r = \rho\dot{R}^2 d_0/\sigma$ is the rim Weber number (which represents the competition between the radial momentum induced at droplet periphery and restoring surface tension of the stable droplet). The term $\dot{R} = U\sqrt{\rho_a/\rho}$ represents the constant radial expansion rate of a droplet (Marcotte & Zaleski 2019). Here, U is the average velocity of the airstream.

The volume weight of the bag, w_B, is given by

$$w_B = \frac{V_B}{V_0} = 1 - \frac{V_N}{V_0} - \frac{V_R}{V_0}. \tag{3.12}$$

The method described above only provides volume weights for each mode. To obtain individual distributions as well as an overall distribution, characteristic droplet sizes must be determined for each mode. We, therefore, address the estimation of characteristic sizes for each mode in the following sections.

3.2.1. *Node droplet sizes (d_N)*

The nodes are formed on the rim due to the Rayleigh–Taylor (RT) instability (Zhao *et al.* 2010) as the lighter fluid (air phase) pushes the heavier fluid (liquid phase). The droplet size (d_N) resulting from the breakup of nodes based on the RT instability theory is given by (Jackiw & Ashgriz 2022)

$$\frac{d_N}{d_0} = \left[\frac{3}{2}\left(\frac{h_i}{d_0}\right)^2 \frac{\lambda_{RT}}{d_0} n\right]^{1/3}, \tag{3.13}$$

where $n = V_N/V_D$ represents the volume fraction of the nodes relative to the disk. Jackiw & Ashgriz (2022) estimated that the minimum, mean and maximum values of n are 0.2, 0.4 and 1, respectively. The three characteristics sizes of node droplets can be determined using these three values of n. The number-based mean and standard deviation for the breakup of the nodes are evaluated from the above-mentioned three characteristic sizes. In (3.13), the

maximum susceptible wavelength of the RT instability, $\lambda_{RT} = 2\pi\sqrt{3\sigma/\rho a}$, wherein

$$a = \frac{3}{4} C_D \frac{U^2}{d_0} \frac{\rho_a}{\rho} (D_{max}/d_0)^2 \tag{3.14}$$

is the acceleration of the deforming droplet. As suggested by Zhao *et al.* (2010), the drag coefficient (C_D) of the disk shape droplet is approximately 1.2 and the extent of droplet deformation, $D_{max}/d_0 = 2/(1 + \exp(-0.0019We^{2.7}))$.

3.2.2. *Rim droplet sizes (d_R)*

The satellite droplets associated with the rim breakup are due to the Rayleigh–Plateau instability, the receding rim instability (Jackiw & Ashgriz 2022) and the nonlinear instability of liquid ligaments near the pinch-off point.

The satellite droplets size (d_R) due to the Rayleigh–Plateau instability mechanism is

$$\frac{d_R}{d_0} = 1.89 \frac{h_f}{d_0}. \tag{3.15}$$

Here, h_f is the final rim thickness, which is given by

$$\frac{h_f}{d_0} = \frac{h_i}{d_0} \sqrt{\frac{R_i}{R_f}}, \tag{3.16}$$

where R_f is the bag radius at the time of its burst. In case of swirl flow, R_f can be evaluated as (Kirar *et al.* 2022)

$$R_f = \frac{d_0}{2\eta} \left[2e^{\tau'\sqrt{p}} + \left(\frac{\sqrt{p}}{\sqrt{q}} - 1 \right) e^{-\tau'\sqrt{q}} - \left(\frac{\sqrt{p}}{\sqrt{q}} + 1 \right) e^{\tau'\sqrt{q}} \right], \tag{3.17}$$

where $\eta = f^2 - 120/We$, $p = f^2 - 96/We$ and $q = 24/We$. Kirar *et al.* (2022) observed that the values of the stretching factor for the no-swirl case, $Sw = 0.47$ and $Sw = 0.82$ are $f = 2.82$, 3.04 and 3.41, respectively. In (3.17), the dimensionless time, $\tau' = t_b/t_d$, where t_b and t_d are the bursting time and characteristic deformation time, respectively. They are given by (Jackiw & Ashgriz 2022)

$$t_b = \frac{\left[\left(\frac{2R_i}{d_0} \right) - 2 \left(\frac{h_i}{d_0} \right) \right]}{\frac{2\dot{R}}{d_0}} \left[-1 + \sqrt{1 + C \frac{8t_d}{\sqrt{3We}} \frac{\frac{2\dot{R}}{d_0}}{\left[\left(\frac{2R_i}{d_0} \right) - 2 \left(\frac{h_i}{d_0} \right) \right]} \sqrt{\frac{V_B}{V_0}}} \right], \tag{3.18}$$

where $C = 9.4$ (Jackiw & Ashgriz 2022) and

$$t_d = \frac{d_0}{U} \sqrt{\frac{\rho}{\rho_a}}. \tag{3.19}$$

The second mechanism responsible for the rim breakup is the receding rim instability (Jackiw & Ashgriz 2022), which results in a droplet size (d_{rr}) as given by

$$\frac{d_{rr}}{d_0} = \left[\frac{3}{2} \left(\frac{h_f}{d_0} \right)^2 \frac{\lambda_{rr}}{d_0} \right]^{1/3}, \tag{3.20}$$

where λ_{rr} is the wavelength of the receding rim instability, which is given by $\lambda_{rr} = 4.5 b_{rr}$. Here, $b_{rr} = \sqrt{\sigma/\rho a_{rr}}$ is the receding rim thickness, $a_{rr} = U_{rr}^2/R_f$ is the acceleration of the

receding rim (Wang *et al.* 2018) and U_{rr} is the receding rim velocity, which is measured experimentally.

The rim breakup occurs due to the nonlinear instability of liquid ligaments near the pinch-off point. To obtain the characteristic size associated with this mechanism, we need to consider both the Rayleigh–Plateau and receding rim instabilities, which are given by (Keshavarz *et al.* 2020)

$$d_{sat,R} = \frac{d_R}{\sqrt{2 + 3Oh_R/\sqrt{2}}} \tag{3.21}$$

and

$$d_{sat,rr} = \frac{d_{rr}}{\sqrt{2 + 3Oh_R/\sqrt{2}}}, \tag{3.22}$$

respectively. Here, $Oh_R = \mu/\sqrt{\rho h_f^3 \sigma}$ is the Ohnesorge number based on the final rim thickness. The characteristic sizes given in (3.15), (3.20), (3.21) and (3.22) are used to evaluate the number-based mean and standard deviation for the rim breakup.

3.2.3. *Bag droplet sizes (d_B)*

The factors that are responsible for the droplet size distribution due to rupture of bag-film are the minimum bag thickness, the receding rim thickness (b_{rr}), the Rayleigh–Plateu instability and nonlinear instability of liquid ligaments. These factors lead to four characteristic sizes of the satellite droplets, which are given by (Jackiw & Ashgriz 2022)

$$d_B = h_{min}, \tag{3.23}$$

$$d_{rr,B} = b_{rr}, \tag{3.24}$$

$$d_{RP,B} = 1.89 b_{rr}, \tag{3.25}$$

$$d_{sat,B} = \frac{d_{RP,B}}{\sqrt{2 + 3Oh_{rr}/\sqrt{2}}}. \tag{3.26}$$

Jackiw & Ashgriz (2022) found that $h_{min} = \pm 2.3\,\mu\text{m}$ for the no-swirl case. Here, $Oh_{rr} = \mu/\sqrt{\rho b_{rr}^3 \sigma}$ is the Ohnesorge number based on receding rim thickness, b_{rr}. These characteristic sizes are used to estimate the number mean and standard deviation associated with the bag fragmentation mode.

Figure 11 shows the volume probability density of droplets for the low-swirl ($Sw = 0.47$) case at a typical instant, $\tau = 0.75$ (this corresponds to the instant at which the fragmentation ceases). The uncertainty in the droplet size distributions from three experimental repetitions is presented in figure S5 of the supplementary material. The corresponding holography and shadowgraphy images are depicted in figure 7. As evident from the size distribution shown in figure 11, there are two distinct modes for the low-swirl case ($Sw = 0.47$). It is to be noted that for retracting bag breakup, the bag fragmentation does not contribute to the size distribution. Therefore, only two geometries, the rim and node, contribute to the overall size distribution. In this case, due to the capillary instability, the breakup of the rim generates smaller droplets with a distribution peak at $d/d_0 \approx 0.20$, while the node breakup due to the Rayleigh–Taylor instability contributes to the droplet size distribution with a peak at $d/d_0 \approx 0.55$. Despite the fact that the rim breakup produces more small droplets (as seen in figure 7 at $\tau = 0.75$) than the

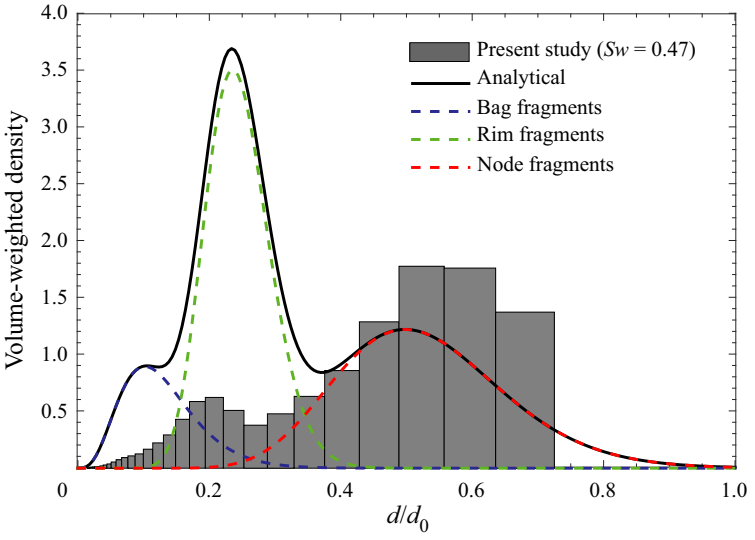

Figure 11. Volume-weighted density of all fragments at $\tau = 0.75$ for $Sw = 0.47$ and $We = 12.1$. This depicts a bi-modal distribution.

node breakup, their contribution to the volume-weighted distribution is smaller since the volume is proportional to the cube of the droplet diameter. To the best of the author's knowledge, this is the first experimental study that reveals a bi-modal distribution for the retracting bag breakup phenomenon. To theoretically predict the size distribution, we use the aforementioned model (Jackiw & Ashgriz 2022) by considering bag, rim and node breakup mechanisms. However, in this scenario, the bag breakup does not produce the satellite droplets and there are additional mechanisms present, such as total bag retraction and partial trapping of the rim in the wake zone of the airstream. We found that while the model reasonably predicts node breakup, it could not predict the size distribution for the bag and rim breakup processes.

In figure 12, we compare the analytical prediction of the combined distribution with the experimental results of the present study for the high swirl strength. Figure S6 in the supplementary material presents the uncertainty in the droplet size distributions obtained using three experimental repetitions. We observe that, unlike the low swirl ($Sw = 0.47$), the high swirl ($Sw = 0.82$) exhibits three distinct modes in the size distribution obtained experimentally, as shown in figure 12. As explained earlier, for the high-swirl case, the entire disk remains in the high-shear zone. Therefore, the disk undergoes the normal bag breakup process, which involves the breakup of inflated bag, rim and nodes. As a result, all these processes contribute to the overall size distribution. The first peak at $d/d_0 \approx 0.14$ in figure 12 is attributed to the bag breakup phenomenon. The second peak observed at $d/d_0 \approx 0.24$ is due to the fragmentation of the rim and the third peak at $d/d_0 \approx 0.45$ is due to the nodes breakup. As explained above, we have analytically calculated the characteristic sizes of each mode (bag, rim and nodes) and then evaluated the individual size distribution of each mode separately. The theoretically predicted combined multi-modal distribution and that for the individual modes are shown in figure 12. The solid line indicates the sum of all the modes (bag+rim+nodes) of the size distribution, while the dashed lines represent the individual modes. These results reveal that the contributions of the bag and rim to the volume-weight size distributions are over-predicted, whereas the contribution to node breakup is under-estimated. However, the theoretically

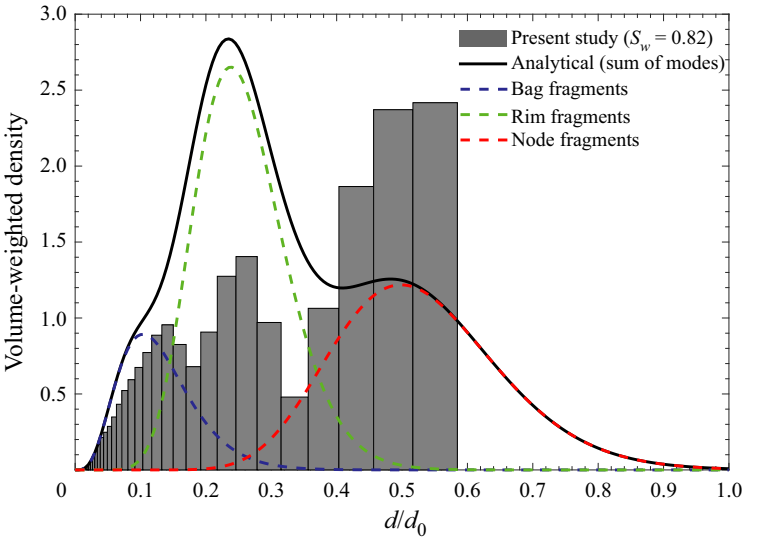

Figure 12. Comparison of the volume-weighted density obtained from our experiments with the theoretical prediction (Jackiw & Ashgriz 2022) at $\tau = 0.66$ for $Sw = 0.82$ and $We = 12.1$. Note the multi-modal distribution is likely due to fragments from the bag, the rim and the node.

predicted characteristic sizes are in reasonable agreement with the experimental results. Therefore, this study demonstrates that the mode shapes and characteristic sizes can be estimated even for the bag breakup of a droplet under a swirl flow. Based on the current experimental data for the high-swirl case, if we consider all the droplets larger than droplet size $d/d_0 = 0.16$ to originate from rim and nodes, the total volume fraction of rim and nodes droplets is 78 % (approximately). For the droplet fragmentation in an airstream without a swirl, Guildenbecher *et al.* (2017) and Gao *et al.* (2013*a*) have reported the total volume fraction of the droplets resulting from rim and nodes breakups to be ∼88 % and ∼90 %, respectively.

4. Concluding remarks

The shape and size distribution of raindrops are important factors in rainfall modelling, which are influenced by several microphysical processes, such as fragmentation, coalescence and phase change. In the present study, we examine the size distribution of satellite droplets produced by the interaction of a freely falling water droplet with a swirl airstream of different strengths using shadowgraphy and digital in-line holography techniques. The Weber number, which measures the aerodynamic force exerted on a droplet by the airstream, is considered to be low enough that the droplet undergoes vibrational breakup, producing only a few satellite droplets of comparable sizes in the no-swirl airstream. As we increase the swirl strength, the water droplet experiences the retracting bag breakup and normal breakup phenomena for $Sw = 0.47$ (low swirl strength) and $Sw = 0.82$ (high swirl strength), respectively. While Kirar *et al.* (2022) observed similar morphological changes for an ethanol droplet, they did not examine the size distribution of the satellite droplets following fragmentation, which is the subject of the current investigation. The digital in-line holography employed to obtain the size distributions of satellite droplets is a deep-learning-based image processing method that has recently emerged as a powerful tool for capturing three-dimensional information with

high spatial resolution. Therefore, it is a more appropriate approach to be employed in the current study for the analysis of the size distribution of satellite droplets produced by fragmentation of a water droplet in a swirling airstream.

We observe that the number mean diameter of the satellite droplets increases over time due to the decrease in the relative velocity between the air and liquid bulk during the fragmentation process. In the high-swirl case ($Sw = 0.82$), the disintegration of the bag, rim and nodes leads to smaller satellite droplets, whereas in the low-swirl scenario ($Sw = 0.47$), the fragmentation of the rim and nodes leads to larger satellite droplets. The bag rupture does not contribute to the size distribution for the low-swirl case. The temporal variations of the Sauter mean diameter reveals that for a given aerodynamic force, a high swirl strength creates more surface area (and thus more surface energy) than a low swirl strength.

A statistical theoretical analysis, similar to that of Villermaux & Bossa (2009) originally developed for a straight airstream without swirl, is also carried out to determine the size distribution of droplets for various swirl strengths. Despite not accounting for all breakup modes, the statistical model predicts the experimental result for small droplets but differs from the results for large droplets when the swirl strength is low. In the case of low swirl number, additional mechanisms such as entrapment of disk in the wake zone of the swirler and absence of bag fragmentation result in larger droplets.

Furthermore, we have analytically evaluated the combined multi-modal distribution that accounts for nodes, rim and bag breakup modes of a droplet in a swirl airflow. In sharp contrast to the earlier studies on the fragmentation of a droplet in a straight airstream without a swirl that observed a monomodal size distribution, we observed bimodal and multi-model distributions for low and high swirl strengths, respectively. We observe two distinct modes for the low swirl scenario ($Sw = 0.47$) due to the rim breakup driven by the capillary instability, which results in smaller droplets with a symmetric distribution, and the subsequent node breakup, which generates an asymmetrical size distribution. For $Sw = 0.47$, we found that the deviations between experiments and the theoretical model predictions in the characteristic size of the droplets owing to the rim and node breakups are approximately 30 % and 16 %, respectively. In contrast, in the high-swirl scenario ($Sw = 0.82$), we observe three peaks in the size distribution due to the breakup of the bag, rim and nodes. Although the theoretically evaluated characteristic sizes are in reasonable agreement with the experimental results, the volume-weighted contributions of the bag and rim are over-predicted, whereas the contribution to node breakup is under-predicted. Quantitatively, for $Sw = 0.82$, the deviations between experiments and the theoretical model predictions in the characteristic size of the droplets due to the bag, rim and node fragmentation are approximately 25 %, 4 % and 4 %, respectively. Nevertheless, the present study is a first attempt to estimate the size distribution of satellite droplets under a swirl airstream, which is observed in many natural and industrial applications.

Supplementary material and movies. Supplementary material and movies are available at https://doi.org/10.1017/jfm.2022.1028.

Funding. L.D.C. and K.C.S. thank the Science & Engineering Research Board, India for their financial support through grants SRG/2021/001048 and CRG/2020/000507, respectively. We thank IIT Hyderabad for the financial support through grant IITH/CHE/F011/SOCH1. S.S.A. also acknowledges the PMRF Fellowship.

Declaration of interests. The authors report no conflict of interest.

Author ORCIDs.
Lakshmana Dora Chandrala https://orcid.org/0000-0002-2695-9469;
Kirti Chandra Sahu https://orcid.org/0000-0002-7357-1141.

References

Agrawal, M., Katiyar, R.K., Karri, B. & Sahu, K.C. 2020 Experimental investigation of a nonspherical water droplet falling in air. *Phys. Fluids* **32** (11), 112105.

Agrawal, M., Premlata, A.R., Tripathi, M.K., Karri, B. & Sahu, K.C. 2017 Nonspherical liquid droplet falling in air. *Phys. Rev.* E **95** (3), 033111.

Apte, S.V., Mahesh, K., Gorokhovski, M. & Moin, P. 2009 Stochastic modeling of atomizing spray in a complex swirl injector using large eddy simulation. *Proc. Combust. Inst.* **32** (2), 2257–2266.

Balla, M., Tripathi, M.K. & Sahu, K.C. 2019 Shape oscillations of a nonspherical water droplet. *Phys. Rev.* E **99** (2), 023107.

Beér, J.M. 1974 Combustion aerodynamics. In *Combustion Technology* (ed. H.B. Palmer & J.M. Beér), pp. 61–89. Elsevier.

Bentley, W.A. 1904 Studies of raindrops and raindrop phenomena. *Mon. Weath. Rev.* **32**, 450–456.

Berg, M.J. 2022 Tutorial: aerosol characterization with digital in-line holography. *J. Aerosol Sci.* **165**, 106023.

Candel, S., Durox, D., Schuller, T., Bourgouin, J.F. & Moeck, J.P. 2014 Dynamics of swirling flames. *Annu. Rev. Fluid Mech.* **46**, 147–173.

Cao, X.K., Sun, Z.G., Li, W.F., Liu, H.F. & Yu, Z.H. 2007 A new breakup regime of liquid drops identified in a continuous and uniform air jet flow. *Phys. Fluids* **19** (5), 057103.

Chaitanya, G.S., Sahu, K.C. & Biswas, G. 2021 A study of two unequal-sized droplets undergoing oblique collision. *Phys. Fluids* **33** (2), 022110.

Dai, Z. & Faeth, G.M. 2001 Temporal properties of secondary drop breakup in the multimode breakup regime. *Intl J. Multiphase Flow* **27** (2), 217–236.

Falk, T., *et al.* 2019 U-Net: deep learning for cell counting, detection, and morphometry. *Nat. Meth.* **16** (1), 67–70.

Gao, J., Guildenbecher, D.R., Reu, P.L. & Chen, J. 2013*a* Uncertainty characterization of particle depth measurement using digital in-line holography and the hybrid method. *Opt. Express* **21** (22), 26432–26449.

Gao, J., Guildenbecher, D.R., Reu, P.L., Kulkarni, V., Sojka, P.E. & Chen, J. 2013*b* Quantitative, three-dimensional diagnostics of multiphase drop fragmentation via digital in-line holography. *Opt. Lett.* **38** (11), 1893–1895.

Gao, P., Wang, J., Gao, Y., Liu, J. & Hua, D. 2022 Observation on the droplet ranging from 2 to 16 μm in cloud droplet size distribution based on digital holography. *Remote Sens.* **14** (10), 2414.

Guildenbecher, D.R., Gao, J., Chen, J. & Sojka, P.E. 2017 Characterization of drop aerodynamic fragmentation in the bag and sheet-thinning regimes by crossed-beam, two-view, digital in-line holography. *Intl J. Multiphase Flow* **94**, 107–122.

Guildenbecher, D.R., Gao, J., Reu, P.L. & Chen, J. 2013 Digital holography simulations and experiments to quantify the accuracy of 3d particle location and 2d sizing using a proposed hybrid method. *Appl. Opt.* **52** (16), 3790–3801.

Guildenbecher, D.R., López-Rivera, C. & Sojka, P.E. 2009 Secondary atomization. *Exp. Fluids* **46** (3), 371–402.

Haan, F.L. Jr., Sarkar, P.P., Kopp, G.A. & Stedman, D.A. 2017 Critical wind speeds for tornado-induced vehicle movements. *J. Wind Engng Ind. Aerodyn.* **168**, 1–8.

Hanson, A.R., Domich, E.G. & Adams, H.S. 1963 Shock tube investigation of the breakup of drops by air blasts. *Phys. Fluids* **6** (8), 1070–1080.

Hsiang, L.P. & Faeth, G.M. 1993 Drop properties after secondary breakup. *Intl J. Multiphase Flow* **19** (5), 721–735.

Ibtehaz, N. & Rahman, M.S. 2020 MultiResUNet: rethinking the U-Net architecture for multimodal biomedical image segmentation. *Neural Netw.* **121**, 74–87.

Jackiw, I.M. & Ashgriz, N. 2021 On aerodynamic droplet breakup. *J. Fluid Mech.* **913**, A33.

Jackiw, I.M. & Ashgriz, N. 2022 Prediction of the droplet size distribution in aerodynamic droplet breakup. *J. Fluid Mech.* **940**, A17.

Jain, M., Prakash, R.S., Tomar, G. & Ravikrishna, R.V. 2015 Secondary breakup of a drop at moderate weber numbers. *Proc. R. Soc. Lond.* A **471** (2177), 20140930.

Katz, J. & Sheng, J. 2010 Applications of holography in fluid mechanics and particle dynamics. *Annu. Rev. Fluid Mech.* **42** (1), 531–555.

Keshavarz, B., Houze, E.C., Moore, J.R., Koerner, M.R. & McKinley, G.H. 2020 Rotary atomization of newtonian and viscoelastic liquids. *Phys. Rev. Fluids* **5** (3), 033601.

Kirar, P.K., Soni, S.K., Kolhe, P.S. & Sahu, K.C. 2022 An experimental investigation of droplet morphology in swirl flow. *J. Fluid Mech.* **938**, A6.

KOSTINSKI, A.B. & SHAW, R.A. 2009 Raindrops large and small. *Nat. Phys.* **5** (9), 624–625.
KRZECZKOWSKI, S.A. 1980 Measurement of liquid droplet disintegration mechanisms. *Intl J. Multiphase Flow* **6** (3), 227–239.
KULKARNI, V. & SOJKA, P.E. 2014 Bag breakup of low viscosity drops in the presence of a continuous air jet. *Phys. Fluids* **26** (7), 072103.
KUMAR, S.S., LI, C., CHRISTEN, C.E., HOGAN, C.J. JR., Fredericks, S.A. & Hong, J. 2019 Automated droplet size distribution measurements using digital inline holography. *J. Aerosol Sci.* **137**, 105442.
KUMAR, A. & SAHU, S. 2019 Large scale instabilities in coaxial air-water jets with annular air swirl. *Phys. Fluids* **31** (12), 124103.
VON LENARD, P. 1904 Über regen. *Meteorol.* Z **6** (249), 92–62.
LEWELLEN, D.C., LEWELLEN, W.S. & XIA, J. 2000 The influence of a local swirl ratio on tornado intensification near the surface. *J. Atmos. Sci.* **57** (4), 527–544.
LI, J., SHEN, S., LIU, J., ZHAO, Y., LI, S. & TANG, C. 2022 Secondary droplet size distribution upon breakup of a sub-milimeter droplet in high speed cross flow. *Intl J. Multiphase Flow* **148**, 103943.
MARCOTTE, F. & ZALESKI, S. 2019 Density contrast matters for drop fragmentation thresholds at low Ohnesorge number. *Phys. Rev. Fluids* **4** (10), 103604.
MARMOTTANT, P. & VILLERMAUX, E. 2004 On spray formation. *J. Fluid Mech.* **498**, 73–111.
MARSHALL, J.S. & PALMER, W.M. 1948 The distribution of raindrops with size. *J. Meteorol.* **5**, 165–166.
MERKLE, K., HAESSLER, H., BÜCHNER, H. & ZARZALIS, N. 2003 Effect of co-and counter-swirl on the isothermal flow-and mixture-field of an airblast atomizer nozzle. *Intl J. Heat Fluid Flow* **24** (4), 529–537.
PATIL, S. & SAHU, S. 2021 Air swirl effect on spray characteristics and droplet dispersion in a twin-jet crossflow airblast injector. *Phys. Fluids* **33** (7), 073314.
PILCH, M. & ERDMAN, C.A. 1987 Use of breakup time data and velocity history data to predict the maximum size of stable fragments for acceleration-induced breakup of a liquid drop. *Intl J. Multiphase Flow* **13** (6), 741–757.
RAJAMANICKAM, K. & BASU, S. 2017 On the dynamics of vortex–droplet interactions, dispersion and breakup in a coaxial swirling flow. *J. Fluid Mech.* **827**, 572–613.
RONNEBERGER, O., FISCHER, P. & BROX, T. 2015 U-net: Convolutional networks for biomedical image segmentation. In *Lecture Notes in Computer Science (including subseries Lecture Notes in Artificial Intelligence and Lecture Notes in Bioinformatics)* (ed. N. Navab, J. Hornegger, W. Wells & A. Frangi), vol. 9351, pp. 234–241. Springer.
SCHLOTTKE, J. & WEIGAND, B. 2008 Direct numerical simulation of evaporating droplets. *J. Comput. Phys.* **227** (10), 5215–5237.
SHANMUGADAS, K.P., CHAKRAVARTHY, S.R., CHIRANTHAN, R.N., SEKAR, J. & KRISHNASWAMI, S. 2018 Characterization of wall filming and atomization inside a gas-turbine swirl injector. *Exp. Fluids* **59** (10), 151.
SHAO, C., LUO, K., CHAI, M. & FAN, J. 2018 Sheet, ligament and droplet formation in swirling primary atomization. *AIP Adv.* **8** (4), 045211.
SHAO, S., MALLERY, K., KUMAR, S.S. & HONG, J. 2020 Machine learning holography for 3d particle field imaging. *Opt. Express* **28** (3), 2987–2999.
SONI, S.K., KIRAR, P.K., KOLHE, P. & SAHU, K.C. 2020 Deformation and breakup of droplets in an oblique continuous air stream. *Intl J. Multiphase Flow* **122**, 103141.
SONI, S.K. & KOLHE, P.S. 2021 Liquid jet breakup and spray formation with annular swirl air. *Intl J. Multiphase Flow* **134**, 103474.
SRIVASTAVA, R.C. 1971 Size distribution of raindrops generated by their breakup and coalescence. *J. Atmos. Sci.* **28** (3), 410–415.
SURYAPRAKASH, R. & TOMAR, G. 2019 Secondary breakup of drops. *J. Indian I. Sci.* **99** (1), 77–91.
SZAKALL, M., DIEHL, K., MITRA, S.K. & BORRMANN, S. 2009 A wind tunnel study on the shape, oscillation, and internal circulation of large raindrops with sizes between 2.5 and 7.5 mm. *J. Atmos. Sci.* **66** (3), 755–765.
TAYLOR, G.I. 1963 The shape and acceleration of a drop in a high speed air stream. *Sci. Pap. GI Taylor* **3**, 457–464.
VILLERMAUX, E. 2007 Fragmentation. *Annu. Rev. Fluid Mech.* **39**, 419–446.
VILLERMAUX, E. & BOSSA, B. 2009 Single-drop fragmentation determines size distribution of raindrops. *Nat. Phys.* **5** (9), 697–702.
VILLERMAUX, E. & ELOI, F. 2011 The distribution of raindrops speeds. *Geophys. Res. Lett.* **38** (19), L19805.
WANG, C., CHANG, S., WU, H. & XU, J. 2014 Modeling of drop breakup in the bag breakup regime. *Appl. Phys. Lett.* **104** (15), 154107.

WANG, Y., DANDEKAR, R., BUSTOS, N., POULAIN, S. & BOUROUIBA, L. 2018 Universal rim thickness in unsteady sheet fragmentation. *Phys. Rev. Lett.* **120** (20), 204503.

WIERZBA, A. 1990 Deformation and breakup of liquid drops in a gas stream at nearly critical Weber numbers. *Exp. Fluids* **9** (1–2), 59–64.

XU, Z., WANG, T. & CHE, Z. 2022 Droplet breakup in airflow with strong shear effect. *J. Fluid Mech.* **941**, A54.

ZHAO, H., LIU, H.F., LI, W.F. & XU, J.L. 2010 Morphological classification of low viscosity drop bag breakup in a continuous air jet stream. *Phys. Fluids* **22** (11), 114103.